






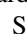







Publication Year	2018
Acceptance in OA@INAF	2020-12-30T10:27:30Z
Title	The 3CR Chandra Snapshot Survey: Extragalactic Radio Sources with Redshifts between 1 and 1.5
Authors	Stuardi, C.; Missaglia, V.; Massaro, F.; Ricci, F.; LIUZZO, Elisabetta Teodorina; et al.
DOI	10.3847/1538-4365/aaafcf
Handle	http://hdl.handle.net/20.500.12386/29338
Journal	THE ASTROPHYSICAL JOURNAL SUPPLEMENT SERIES
Number	235



The 3CR *Chandra* Snapshot Survey: Extragalactic Radio Sources with Redshifts between 1 and 1.5

C. Stuardi^{1,2,3,4} , V. Missaglia⁵, F. Massaro^{2,3,6} , F. Ricci^{7,8} , E. Liuzzo⁴ , A. Paggi⁸ , R. P. Kraft⁸ , G. R. Tremblay⁸ , S. A. Baum^{9,10} , C. P. O’Dea^{9,11} , B. J. Wilkes⁸ , J. Kuraszkiewicz⁸, W. R. Forman⁸ , and D. E. Harris^{8,12}

¹ Dipartimento di Fisica e Astronomia, Università di Bologna, via Piero Gobetti 93/2, I-40129 Bologna, Italy

² Dipartimento di Fisica, Università degli Studi di Torino, via Pietro Giuria 1, I-10125 Torino, Italy

³ INAF-Osservatorio Astrofisico di Torino, via Osservatorio 20, I-10025 Pino Torinese, Italy

⁴ Istituto di Radioastronomia, INAF, via Gobetti 101, I-40129, Bologna, Italy

⁵ Department of Physical Sciences, University of Napoli Federico II, via Cinthia 9, I-80126 Napoli, Italy

⁶ Istituto Nazionale di Fisica Nucleare, Sezione di Torino, I-10125 Torino, Italy

⁷ Dipartimento di Matematica e Fisica, Università Roma Tre, via della Vasca Navale 84, I-00146, Roma, Italy

⁸ Smithsonian Astrophysical Observatory, 60 Garden Street, Cambridge, MA 02138, USA

⁹ University of Manitoba, Dept. of Physics and Astronomy, Winnipeg, MB R3T 2N2, Canada

¹⁰ Center for Imaging Science, Rochester Institute of Technology, 84 Lomb Memorial Dr., Rochester, NY 14623, USA

¹¹ School of Physics & Astronomy, Rochester Institute of Technology, 84 Lomb Memorial Dr., Rochester, NY 14623, USA

Received 2017 October 16; revised 2018 February 8; accepted 2018 February 13; published 2018 April 2

Abstract

The aim of this paper is to present an analysis of newly acquired X-ray observations of 16 extragalactic radio sources listed in the Third Cambridge Revised (3CR) catalog and not previously observed by *Chandra*. Observations were performed during *Chandra* Cycle 17, extending X-ray coverage for the 3CR extragalactic catalog up to $z = 1.5$. Among the 16 targets, two lie at $z < 0.5$ (3CR 27 at $z = 0.184$ and 3CR 69 at $z = 0.458$); all of the remaining 14 have redshifts between 1.0 and 1.5. In the current sample, there are three compact steep spectrum (CSS) sources, three quasars, and an FR I radio galaxy, while the other nine are FR II radio galaxies. All radio sources have an X-ray counterpart. We measured nuclear X-ray fluxes as well as X-ray emission associated with radio jet knots, hotspots, or lobes in three energy bands: soft (0.5–1 keV), medium (1–2 keV), and hard (2–7 keV). We also performed standard X-ray spectral analysis for the four brightest nuclei. We discovered X-ray emission associated with the radio lobe of 3CR 124, a hotspot of the quasar 3CR 220.2, another hotspot of the radio galaxy 3CR 238, and the jet knot of 3CR 297. We also detected extended X-ray emission around the nuclear region of 3CR 124 and 3CR 297 on scales of several tens of kiloparsecs. Finally, we present an update on the X-ray observations performed with *Chandra* and *XMM-Newton* on the entire 3CR extragalactic catalog.

Key words: galaxies: active – radio continuum: galaxies – X-rays: general

1. Introduction

The last revised version of the Third Cambridge catalog (3CR) of extragalactic radio sources (Spinrad et al. 1985) remains one of the best-studied samples of radio-loud active galactic nuclei (AGNs) and is critical for statistical analysis of their properties (see, e.g., Shields 1999; Tadhunter 2016). The 3CR catalog is a 178 MHz radio flux-limited sample, with a 9 Jy cutoff, that covers the redshift range $0.0005 < z < 2.5$. As a low frequency selected sample, it is unbiased with respect to viewing angle, X-ray properties (e.g., total X-ray nuclear flux and spectrum), and optical spectroscopic classification of the sources.

In recent years, the large majority of the 298 3CR extragalactic sources have been observed with several photometric and spectroscopic surveys, in the radio, infrared (IR), and optical wave bands, so that a vast suite of data is now available to facilitate multifrequency analyses. Radio images with arcsecond resolution for the majority of the 3CR sources are available from the National Radio Astronomy Observatory Very Large Array (VLA) Archive Survey (NVAS) and in the archive of the MERLIN observatory. Recently, several snapshot surveys of 3CR radio sources were carried out using the *Spitzer* satellite (see, e.g., Dicken et al. 2014; Ramírez et al. 2014; Ghaffari et al. 2017) and

the *Hubble Space Telescope* (*HST*; see, e.g., Privon et al. 2008; Tremblay et al. 2009), reaching a coverage of about 90% of the entire extragalactic catalog including new observations of high-redshift sources at $z > 1.0$ (see also Leipski et al. 2010; Hilbert et al. 2016). Several high-redshift 3CR radio galaxies and quasars were detected in the far-infrared also by the *Herschel Space Observatory* (Podigachoski et al. 2016). Moreover, ground-based spectroscopic observations were carried out with the Telescopio Nazionale Galileo (Buttiglione et al. 2009, 2011).

To extend the wavelength coverage of the 3CR catalog, we started an X-ray snapshot survey with *Chandra*, the only X-ray facility with angular resolution comparable to that at optical and radio frequencies (see Massaro et al. 2015 for a recent review). The main aims of the *Chandra* snapshot survey can be summarized as follows: (1) study the X-ray emission, as a function of z and radio power, arising from jet knots, hotspots, and nuclei of radio sources; (2) investigate the nature of their large-scale environment; and (3) search for observational evidence of AGN interactions with the hot gas in galaxies, groups, and clusters of galaxies. This interaction, known as *feedback*, is observed, for example, in cool-core galaxy clusters, where extended structures (e.g., lobes) of radio sources expand into the X-ray-emitting intracluster medium, creating cavities filled with radio-emitting plasma (see, e.g., Fabian 2012; Kraft et al. 2012). *Chandra* observations also allow us to search for new galaxy clusters via the presence of extended X-ray emission unrelated to the radio structures on kiloparsec and megaparsec scales around the sources

¹² Dan Harris passed away on 2015 December 6th. His career spanned much of the history of radio and X-ray astronomy. His passion, insight, and contributions will always be remembered. A significant fraction of this work is one of his last efforts.

(see, e.g., Belsole et al. 2007; Ineson et al. 2013; Mannering et al. 2013).

Before Cycle 9, only $\sim 60\%$ of 3CR extragalactic sources were observed by *Chandra*: the snapshot survey allowed us to observe 113 more targets, and all those with $z < 1.5$ have at least a snapshot (< 20 ks exposure) observation available in the *Chandra* archive¹³ to date. In the previous subsamples, observed during Cycles 9, 12, 13, and 15, we detected significant X-ray emission from all but two active nuclei and from 22 hotspots (see Massaro et al. 2010, 2012, 2013, 2018). Extended X-ray emission, possibly arising from the hot gas of a surrounding galaxy group or cluster, was also detected around 16 sources. Moreover, the *Chandra* snapshot survey inspired follow-up observations on several interesting objects such as 3CR 171 (Hardcastle et al. 2010), 3CR 305 (Hardcastle et al. 2012), and the tailed radio galaxy 3CR 89 (Dasadia et al. 2016). Our final goal of completing the *Chandra* observational coverage of the entire 3CR extragalactic catalog could be achieved in the next cycle, with the observation of the remaining nine sources.

Here, we present the X-ray analysis of *Chandra* observations carried out during Cycle 17, including 16 3CR radio sources previously unobserved by *Chandra*. Among the 16 targets, 14 are in the redshift range 1.0–1.5, while revised spectroscopic observations yielded an updated redshift estimate for the other two: 3CR 27, $z = 0.184$, and 3CR 69, $z = 0.458$ (Hiltner & Röser 1991).

The paper is organized as follows. A brief description of the observations and data reduction procedures is given in Section 2, while general results and source details are described in Section 3. A brief summary and conclusions are given in Section 4. Finally, we present in Appendix A X-ray images with radio contours overlaid for all of the sources in the current high-redshift sample and in Appendix B the updated summary of X-ray observations, including *Chandra* and *XMM-Newton* information, for the entire 3CR extragalactic portion of the catalog.

Throughout, we assumed a flat cosmology with $H_0 = 69.6 \text{ km s}^{-1} \text{ Mpc}^{-1}$, $\Omega_M = 0.286$, and $\Omega_\Lambda = 0.714$ (Bennett et al. 2014), and we adopted cgs units, unless stated otherwise. Spectral indices, α , are defined by the flux density, $S_\nu \propto \nu^{-\alpha}$.

2. Observations, Data Reduction, and Analysis

We adopted the data reduction and analysis procedures described in previous works, so only basic details are reported here (see, e.g., Massaro et al. 2009b, 2011, for a complete description). We compared radio images, ranging from 1.4 to 14.9 GHz, and *Chandra* observations, searching for a spatial coincidence between X-ray emission and extended radio structures (i.e., jet knots, hotspots, or lobes).

2.1. Radio Observations

Radio images were retrieved from the NVAS¹⁴ and the DRAGN¹⁵ web pages.

For the peculiar case of 3CR 297 (see Section 3), we also computed the radio spectral index map, using archival observations at 4.85 and 8.4 GHz. The radio spectral index, α_R , is a diagnostic tool to obtain useful information on the particle energy distribution of electrons emitting via synchrotron emission. Spatial variations in spectral index across the radio structure were used to

distinguish different regions of 3CR 297, since they could indicate differences in the underlying physical processes occurring in cores and in jets: radio emission arising from compact cores typically has a flat radio spectrum (i.e., $\alpha_R \lesssim 0.5$), while that from extended structures is characterized by a steeper spectrum (see, e.g., Pauliny-Toth & Kellermann 1968).

Archival VLA data analyzed are from project IDs AE0059 (4.85 GHz) and AV0164 (8.4 GHz) and were obtained on 1988 October 30 and 1990 May 11, respectively. In both observing runs, the VLA configuration was A. We performed postcorrelation processing and imaging with the Common Astronomy Software Applications (CASA).

We first calibrated the images in amplitude and phase with the primary calibrators 1127–145 (4.85 GHz) and 1328+307 (8.4 GHz). We set the uv range for the computation of gain solutions in the latter case to a maximum of 400 k λ , following the specification on the VLA fringe calibrators.¹⁶ For the 4.85 GHz data, we flagged the antenna VA20 in the RR correlation in the bin time 14:28:55.0 to remove the bad response and achieve better gain solutions. Then, a self-calibration procedure was iteratively applied to improve the signal-to-noise ratio, using the CASA task `gaincal + applycal`. We obtained the model image through the `clean` task using the weighting parameter set on `natural` first, and `uvtaper` at the end, to model also the extended emission. During this procedure, we flagged additional deviating data (at 8.4 GHz the antenna VA22 for time less than 06:42:00 and VA13 between 07:00:0 and 07:01:15).

We computed the two final continuum maps with the same beam (0 $^{\circ}$ 98, 0 $^{\circ}$ 88, -35° , task `clean` using `uvtaper`), and we regridded both to the same cell size (task `imregrid`) to properly compute the spectral index image for pixels with values $> 3\sigma$ with the relation $\alpha_R = -\log(S_1/S_2)/\log(\nu_1/\nu_2)$, with $\nu_1 = 4.85 \text{ GHz}$, $\nu_2 = 8.4 \text{ GHz}$, and $S_{1,2}$ being the respective flux at the two frequencies (task `immath`). The resulting average rms of the 3CR 297 radio map was 0.4 (0.15) mJy beam $^{-1}$, and the peak flux was 0.510 (0.299) Jy at 4.85 (8.4) GHz. Typical uncertainties for flux density measurements in 3CR 297 radio maps are $\sim 10\%$ for 4.85 GHz and $\sim 3\%$ for 8.4 GHz.

2.2. X-Ray Observations

The 3CR source sample observed during Cycle 17 is listed in Table 1, together with the basic parameters of each source (e.g., radio and optical classification, celestial coordinates, redshift, visual magnitude, and radio flux). Sources were observed for a nominal exposure time of 12 ks, but actual live times are given in Table 2. All *Chandra* observations were performed with the ACIS-S back-illuminated chip in VERY FAINT mode to provide high sensitivity and a low background level. The four chips turned on were I2, I3, S2, and S3 with the nominal aim point centered on S3.

We performed the data reduction following the standard reduction procedure described in the *Chandra* Interactive Analysis of Observations (CIAO) threads,¹⁷ using CIAO version 4.9 and the *Chandra* Calibration Database (CALDB) version 4.7.3. Level 2 event files were generated using the `acis_process_events` task, and events were filtered for grades 0, 2, 3, 4, and 6 and corrected for bad pixels. Light curves for every data set were extracted and checked for high background intervals, but none were found.

¹³ <http://cda.harvard.edu/chaser/>

¹⁴ <https://archive.nrao.edu/nvas>

¹⁵ <http://www.jb.man.ac.uk/atlas/>

¹⁶ <https://science.nrao.edu/facilities/vla/observing/callist>

¹⁷ <http://cxc.harvard.edu/ciao/guides/index.html>

Table 1
Source List of the *Chandra* Cycle 17 Snapshot Survey of 3CR Radio Sources

3CR	Class ^a	R.A. (J2000) ^b (hh mm ss)	Decl. (J2000) ^b (dd mm ss)	z ^c	D_L (Mpc)	Scale (kpc/'')	$N_{H, Gal}$ ^d (10^{20} cm^{-2})	m_v ^e	S_{178} ^f (Jy)	<i>Chandra</i> ObsID	Obs. date (yyyy-mm-dd)
27*	FR II-HERG	00 56 01.0	+68 22 30	0.184	900	3.113	41.2	18.2	26.5	18090	2016 Mar 15
69	FR II-HERG	02 38 02.673	+59 11 50.56	0.458	2577	5.877	68.5	19.0	20.9	18092	2016 Apr 09
36	FR II-HERG	01 17 59.555	+45 36 22.43	1.301	9293	8.510	6.35	20.0 ⁺	8.2	18091	2016 Mar 05
119	CSS	04 32 36.505	+41 38 28.44	1.023	6893	8.166	36.7	20.0 ⁺	15.7	18093	2015 Dec 20
124	FR II-HERG	04 41 59.129	+01 21 01.10	1.083	7399	8.267	8.75	22.0	10.3	18094	2015 Dec 15
173	CSS - HERG	07 02 20.474	+37 57 22.54	1.035	6994	8.187	9.42	21.3 ⁺	8.7	18095	2015 Dec 03
194	FR II-HERG	08 10 03.636	+42 28 05.02	1.184	8266	8.402	4.76	20.0 ⁺	9.9	18096	2015 Dec 17
208.1	QSO	08 54 39.373	+14 05 52.06	1.020 ⁺	6868	8.160	3.35	20.0 ⁺	8.1	18097	2016 Mar 01
220.2	QSO	09 30 33.541	+36 01 25.14	1.157 ⁺	8033	8.370	1.20	19.0 ⁺	7.2	18098	2016 Feb 08
222	FR I	09 36 32.023	+04 22 10.18	1.339	9632	8.535	3.10	23.0 ⁺	11.3	18099	2016 Jan 15
230*	FR II-HERG	09 51 58.8	-00 01 27	1.487	10970	8.599	3.63	...	21.1	18100	2016 Jan 13
238	FR II-HERG	10 11 00.350	+06 24 39.02	1.405 ⁺	10225	8.570	1.96	22.5 ⁺	16.6	18101	2016 Jan 28
255	FR II(?) -HERG	11 19 25.292	-03 02 51.36	1.355	9775	8.545	4.29	23.0	12.5	18102	2016 Feb 07
297*	QSO	14 17 24.0	-04 00 48	1.406 ⁺	10234	8.571	3.29	21.9 ⁺	10.3	18103	2016 Mar 27
300.1	FR II-HERG	14 28 31.230	-01 24 07.04	1.159	8050	8.372	3.13	19.0 ⁺	14.1	18104	2015 Dec 21
305.1*	CSS - LERG	14 47 09.5	+76 56 21	1.132 ⁺	7817	8.338	3.12	21.4 ⁺	4.6	18105	2016 Aug 07

Notes. The two sources above the line are outside the redshift range $1.0 < z < 1.5$.

^a The ‘‘Class’’ column contains both a radio morphology descriptor (Fanaroff–Riley class I or II), quasar (QSO), or compact steep spectrum (CSS) and the optical spectroscopic designation LERG, ‘‘low-excitation radio galaxy,’’ or HERG, ‘‘high-excitation radio galaxy,’’ when present in the literature.

^b The celestial positions listed are those of the radio cores, which we used to register the X-ray images, except for the four sources lacking an obvious radio nucleus: 3CR 27, 3CR 230, 3CR 297, and 3CR 305.1, labeled with ‘‘*,’’ for which the coordinates are taken from the NASA/IPAC Extragalactic Database (NED).

^c Redshift measurements are taken from Spinrad (Spinrad et al. 1985) or from NED. Data from Spinrad are labeled with ‘‘+.’’

^d Galactic neutral hydrogen column densities $N_{H, Gal}$ (Kalberla et al. 2005).

^e m_v is the visual magnitude from Spinrad (Spinrad et al. 1985) or from NED. Data from Spinrad are again labeled with ‘‘+.’’ The value of visual magnitude reported by NED for 3CR 230 is affected by a star nearby in projection on the sky, and it is not reported here.

^f S_{178} is the flux density at 178 MHz (Spinrad et al. 1985).

Since the on-axis width of the point-spread function (PSF) of the *Chandra* telescope is smaller than the size of the ACIS pixels ($0''.492$), to recover the native angular resolution, it is necessary to avoid the undersampling. This is achieved by regridding all of the images to one-fourth of the native size to obtain a common pixel size of $0''.123$.

When possible, we registered X-ray images, changing the appropriate keywords in the header of the event file so as to align the nuclear X-ray position with that of the radio. In most cases, the total angular shift (reported for each registered source in Table 2) was less than $1''$, as occurred in all previous sources analyzed and collected in the XJET website¹⁸ (Massaro et al. 2011). The registration facilitates accurate searches for X-ray emission from within the extended radio structures by comparing radio and X-ray data with similar angular resolution. The distribution of the offsets in Table 2 is consistent with the level of uncertainty in the *Chandra* absolute astrometry ($0''.8$ at 90% confidence, $1''.4$ at 99%).¹⁹ We have also confirmed by eye the identification of the X-ray, radio, and optical nuclei in all cases.

2.2.1. Flux Maps

We created flux maps in three energy ranges: 0.5–1 keV (soft band), 1–2 keV (medium band), and 2–7 keV (hard band), by filtering the event file with the appropriate energy range and taking into account exposure time and effective area. Since the effective area is a function of the photon energy, we created monochromatic exposure maps with nominal energies, E_{nominal} , of 0.8, 1.4, and 4 keV for the soft, medium, and

hard band, respectively. To obtain flux maps in units of $\text{erg cm}^{-2} \text{s}^{-1} \text{pixel}^{-1}$, we multiplied each event by the nominal energy of its respective band. Throughout the paper, we used the regridded pixels of size $0''.123$.

To measure observed fluxes for nuclei and for any X-ray-detected component, we chose an appropriate circular region. For nuclei, we used circular regions of $2''$ radius (see Table 2), while the radius of the circular regions used for other detected components is reported in Table 3. X-ray fluxes were computed using the flux maps for each source region in the three energy ranges previously defined. Since the nominal energy was used only to recover the correct units in the flux maps, for each particular region we applied a correction by multiplying the flux by a factor of $E_{\text{average}}/E_{\text{nominal}}$, where E_{average} is the mean energy computed in the photometric aperture, for the soft, medium, and hard band, respectively. This correction ranged from a few to $\sim 15\%$. For each radio feature, we chose two adjacent source-free background regions, with the same size described above, to avoid contaminating X-ray emission (as well as radio emission) and to sample both sides of the extended radio structure. The 1σ uncertainties on the fluxes were computed using the relative uncertainties on the number of counts, estimated assuming a Poisson distribution and taking into account the background. The background level in the *Chandra* images is sufficiently low that small changes in the background regions used do not result in significant changes in the derived flux uncertainties.

We used the nuclear fluxes measured with this procedure to determine the X-ray hardness ratios (HRs) through the simple relation $(H - M)/(H + M)$, where H and M are the X-ray fluxes in the hard and medium bands, respectively. In Table 2, the uncertainties on the observed value of HR were propagated from

¹⁸ <https://hea-www.harvard.edu/XJET/>

¹⁹ <http://cxc.harvard.edu/cal/ASPECT/celmon/>

Table 2
Nuclear X-Ray Fluxes

3CR	Shift ^a ($''$)	LivTim ^b (ks)	N_2^c (counts)	Ext. ratio ^d	$f(\text{Soft})^e$ 0.5–1 keV	$f(\text{Medium})^e$ 1–2 keV	$f(\text{Hard})^e$ 2–7 keV	$f(\text{Total})^e$ 0.5–7 keV	HR ^f	L_X^g (10^{44} erg s $^{-1}$)
27	–	11.91	61(8)	0.90(0.06)	–	2.3(1.0)	86(11)	88(11)	<0.94	0.09(0.01)
69	0.62	11.92	497(22)	0.94(0.01)	9(2)	74(5)	350(20)	433(21)	0.65(0.03)	3.4(0.2)
36	0.66	11.91	335(18)	0.94(0.01)	27(4)	65(5)	143(13)	235(15)	0.37(0.05)	24.3(1.6)
119	0.60	11.90	383(20)	0.97(0.01)	18(4)	64(5)	220(16)	303(17)	0.54(0.04)	17.2(0.9)
124	0.48	11.92	21(5)	0.49(0.09)	1.5(1.0)	0.5(0.5)	22(5)	24(5)	< 0.96	1.6(0.3)
173	1.10	12.40	124(11)	0.96(0.03)	11(3)	21(3)	43(7)	76(8)	0.34(0.09)	4.4(0.5)
194	0.36	11.91	125(11)	0.87(0.03)	0.8(0.8)	18(3)	89(10)	108(11)	0.67(0.05)	8.8(0.9)
208.1	0.73	11.91	228(15)	0.92(0.02)	25(4)	35(4)	102(11)	162(12)	0.48(0.06)	9.1(0.7)
220.2	0.44	11.92	684(26)	0.94(0.01)	78(7)	119(7)	273(18)	470(20)	0.39(0.04)	36.3(1.5)
222	0.68	11.91	3(2)	–	–	0.8(0.6)	1.5(1.5)	2.3(1.6)	–	0.3(0.2)
230	–	12.35	25(5)	0.7(0.1)	–	2.4(1.0)	21(5)	24(5)	<0.80	3.5(0.7)
238	0.13	11.91	23(5)	0.5(0.1)	2.0(1.0)	3.5(1.2)	8(3)	14(3)	–	1.8(0.4)
255	0.73	11.92	5(2)	–	0.7(0.7)	1.0(0.6)	1.4(1.4)	3.1(1.7)	–	0.4(0.2)
297	0.54	12.34	17(4)	0.24(0.06)	1.3(0.9)	2.5(0.9)	8(3)	12(3)	–	1.5(0.4)
300.1	0.24	11.92	19(4)	0.42(0.09)	0.6(0.6)	0.8(0.6)	22(6)	23(6)	<0.93	1.8(0.5)
305.1	–	11.91	16(4)	0.7(0.2)	0.8(0.8)	–	20(5)	20(5)	<0.92*	1.5(0.4)

Notes. Fluxes are given in units of 10^{-15} erg cm $^{-2}$ s $^{-1}$. Values in parentheses are 1σ uncertainties.

^a Angular shift imposed on the X-ray image to align the nuclear X-ray position with that of the radio. The symbol “–” marks the sources without astrometric registration.

^b LivTim is the observation live time.

^c Total number of counts within a circle of radius $r = 2''$ centered on the source position. The uncertainties given in parentheses are computed as $\sqrt{\text{total-number-of-counts}}$.

^d “Extent ratio”: the ratio of the net counts (i.e., background subtracted) in the $r = 2''$ circle to the net counts in the $r = 10''$ circle. Values less than 0.5 indicate the presence of extended emission around the nuclear component of 3CR 124, 3CR 297, and 3CR 300.1. We did not report values of “extent ratio” for 3CR 222 and 3CR 255, having less than nine counts in the $2''$ circle. A 1σ uncertainty is derived from the Poisson uncertainties on the number of counts in the circular region of radius $2''$ and in the annular region between the radii $2''$ and $10''$, taking into account the covariance of the terms and the uncertainty on the number of background counts measured on the CCD.

^e Fluxes extracted from the flux maps in the three energy bands (0.5–1, 1–2, 2–7 keV) and the total flux in the energy range 0.5–7 keV. The uncertainties are derived from the relative uncertainties on the number of counts in the source and background regions, added in quadrature. The symbol “–” indicates that no counts were detected in the photometric region in the respective energy range.

^f The observed nuclear fluxes have been used to determine the hardness ratios (HR) with the relation $(H - M)/(H + M)$, where H and M are the X-ray fluxes in the hard and medium bands, respectively. We computed the HRs for those sources having more than nine counts in the hard and medium bands, while we only estimated the upper bound of the HR value for those sources with nine or more counts in the hard band alone. The HR upper bound for the source 3CR 305.1, labeled with “*,” was computed with the soft X-ray flux S (i.e., $(H - S)/(H + S)$) due to the lack of counts detected in the medium band. The uncertainties have been derived from the X-ray flux uncertainties.

^g X-ray luminosity in the range 0.5–7 keV, computed using the values of D_L given in Table 1. A 1σ uncertainty is derived from the uncertainties on the flux.

the uncertainties of H and M , taking into account the covariance terms (see, e.g., Park et al. 2006). We did not use the soft-band flux values because they are the most affected by Galactic absorption, except in the case of 3CR 305.1, where no counts were detected in the medium band (see Table 2). We did not compute the HRs for those sources having less than nine counts in each band, while for those with high counts in the hard band alone we estimated the upper bound for the HR values.

Finally, we computed X-ray luminosities using the values of D_L given in Table 1. X-ray fluxes and luminosities for the nuclei are given in Table 2, while those of the detected components are given in Table 3, together with their detection significance evaluated by adopting Poisson statistics. In the latter table, the component classification is indicated by a letter (i.e., hotspot h , lobe l , jet knot k , respectively), a cardinal direction as viewed from the nucleus, and a number indicating the distance from the nucleus in arcseconds (as in Massaro et al. 2011).

2.2.2. X-Ray Spectral Analysis of the Stronger Nuclei

We performed X-ray spectral analysis for the nuclei containing 300 or more total counts to estimate their X-ray spectral indices, α_X . The 400-count threshold adopted in previous

analysis (see, e.g., Massaro et al. 2018) was lowered for this higher redshift sample. We carried out the analysis on the level 2 event files using XSPEC version 12.9 (Arnaud 1996) and CIAO 4.9 SHERPA version 1 (Freeman et al. 2001) software packages, with consistent results.

We extracted the spectral data from the same $2''$ photometric aperture centered around the nuclei described above, using the CIAO routine `specextract`, while the background spectra were extracted in nearby rectangular regions not containing obvious X-ray sources. Then, we binned the background-subtracted spectra to a 30 counts per bin minimum threshold to ensure the validity of the χ^2 statistics, and we selected the energy range 0.5–7 keV for the spectral fitting.

We fitted the photon fluxes of the four brightest sources with a simple multiplicative model, `phabs*powerlaw` in XSPEC syntax: a power law absorbed by the Galactic-equivalent hydrogen column density, $N_{H,\text{Gal}}$ (Table 1, Kalberla et al. 2005). The normalization parameter and the X-ray spectral index, α_X , were allowed to vary. Results of the fit procedure are reported in Table 4.

We also considered the possible presence of mild pileup in *Chandra* observations of the two nuclei with the highest number of counts in our sample: 3CR 69 and 3CR 220.2.

Table 3
Radio Components with X-Ray Detections

3CR	Component ^a	Radius ^b (arcsec)	Total(bkg) ^c (counts)	Detection significance ^d	$f(\text{Soft})^e$ 0.5–1 keV	$f(\text{Medium})^e$ 1–2 keV	$f(\text{Hard})^e$ 2–7 keV	$f(\text{Total})^e$ 0.5–7 keV	L_X^f 10^{44} erg s ⁻¹
124	<i>l-w</i> 8	2.5	5(1)*	$>3\sigma$...	1.2(0.7)	1.9(1.9)	3(2)	0.2(0.1)
220.2	<i>h-s</i> 5	2.0	11(0.3)	$>7\sigma$	1.8(1.1)	0.9(0.7)	4(3)	7(3)	0.5(0.2)
238	<i>h-n</i> 3	2.0	9(0.2)	$>7\sigma$	1.3(0.9)	1.2(0.6)	2.9(1.7)	5(2)	0.7(0.3)
297	<i>k-w</i> 4	2.0	33(0.2)	$>7\sigma$	3.9(1.8)	5.6(1.5)	9(3)	19(4)	2.4(0.5)

Notes. Fluxes are given in units of 10^{-15} erg cm⁻² s⁻¹.

^a The component designation is composed of a letter indicating the classification (i.e., hotspot *h*, lobe *l*, jet knot *k*), a cardinal direction (as viewed from the nucleus), and the distance from the nucleus in arcseconds (as in Massaro et al. 2011).

^b Size of the aperture used for photometry.

^c Total counts in the photometric circle, with the background estimated from the CCD and rescaled on the component region, in parentheses; both counts refer to the total 0.5–7 keV band. In particular, for the source 3CR 124, labeled with “*,” since there is diffuse X-ray emission surrounding the nuclear region, we estimated the local background at the same angular separation of the radio lobe/relic, within an annulus of 5'' inner radius and 10'' outer radius (see also Section 3.3).

^d The confidence level of each detection evaluated adopting a Poisson distribution.

^e Fluxes extracted from the flux maps in the three energy bands (0.5–1, 1–2, 2–7 keV) and the total flux in the energy range 0.5–7 keV. The 1σ uncertainties in parentheses are derived from the uncertainties on the number of counts in the source and background regions, added in quadrature.

^f X-ray luminosity in the range 0.5–7 keV, computed using the values of luminosity distance D_L given in Table 1. A 1σ uncertainty is derived from the uncertainties on the flux, and it is given in parentheses.

Pileup occurs on X-ray CCDs for sources with high flux levels when two or more photons arrive within the same detector pixel within a single CCD frame integration time, and they are counted as a single photon of higher energy.

We first produced pileup maps with the CIAO `pileup_map` tool, which indicated a pileup fraction of $\sim 5\%$ and $\sim 10\%$ in the nuclei of 3CR 69 and 3CR 220.2, respectively. To constrain more precisely the pileup amount in these observations, we performed a spectral fitting with SHERPA, adding to the previous model the `jdpileup` model (Davis 2001). Following the SHERPA thread,²⁰ we fixed the parameters: grade zero probability, $g_0 = 1$; number of detection cells, $n = 1$; and maximum number of photons considered for pileup in a single frame, $n_{\text{terms}} = 30$. In addition, the frame time, f_{time} , and fractional exposure, f_{fracexp} , parameters were fixed to the values of the keywords EXPTIME and FRACEXPO of the event and ARF files. The probability of a good grade when two photons pile together, α , and the fraction of flux falling into the pileup region, f , were left free to vary during the fit.

The power-law spectral index we obtained for 3CR 69 is consistent with the 0.4 value reported in Table 4, obtained without the pileup model, and the pileup fraction as evaluated from the `get_pileup_model` SHERPA command is zero. Since the quality of the data collected for 3CR 36 and 3CR 119, observed to have lower flux levels, is not sufficient to allow a more detailed spectral analysis, we conclude that these sources are affected by a pileup fraction $\lesssim 5\%$ and that the estimate of their spectral index is not compromised.

In the case of 3CR 220.2, the pileup fraction obtained from the spectral fitting with SHERPA is 8.5%, comparable with that evaluated from the pileup map, and the spectral index obtained with the pileup model is reported in Table 4. Although the two values are consistent within the 1σ range, we note that the pileup effect tends to be more severe in this source, hardening the spectrum. The spectral fit performed with the pileup model yields estimates of the flux in the soft, medium, hard, and total bands of 1.3, 1.6, 3.7, and 6.6×10^{-13} erg cm⁻² s⁻¹, respectively. The total source luminosity is 5.1×10^{45} erg s⁻¹.

²⁰ <http://cxc.harvard.edu/sherpa/ahelp/jdpileup.html>

Table 4
Spectral Analysis of Bright Nuclei

3CR	N_2^a	α_X^b	$\chi^2(\text{dof})^c$
36	335(18)	0.7(0.1)	5.68(7)
69	492(22)	0.4(0.1)	21.38(13)
119	381(20)	0.5(0.1)	8.49(9)
220.2 ^d	683(26)	0.60(0.07)	13.7(19)
220.2 ^d	683(26)	$0.81^{+0.08}_{-0.25}$	13.2(17)

Notes. These four nuclei have 300 or more total counts in the photometric aperture and are thus suitable for spectral analysis.

^a Total number of counts within a circle of radius = 2''. The uncertainties given in parentheses are computed as $\sqrt{\text{total-number-of-counts}}$.

^b X-ray spectral index α_X with 1σ uncertainties derived from the fit in parentheses.

^c χ^2 of the fit procedure with degrees of freedom in parentheses.

^d For the source 3CR 220.2, whose observation was found to be affected by a pileup fraction of $\sim 8.5\%$, we reported fit results obtained with the simple model of a power law with Galactic absorption (first row) and with the addition of the `jdpileup` model (second row).

3. Results

3.1. General

In the current sample of 16 X-ray-detected sources, three are classified as compact steep spectrum (CSS) radio sources: 3CR 119, 3CR 173, and 3CR 305.1 (O’Dea 1998). Among the other sources, three are quasars, nine are FR II radio galaxies, and one is an FR I. Radio classifications reported in Table 1 are based on a literature search, with the exception of the radio galaxy 3CR 255, for which we propose an FR II classification.

We detected X-ray emission for all of the nuclei in the sample with a level of significance higher than 3σ . All results of the X-ray photometry (i.e., nuclear X-ray fluxes in the three energy bands, together with their X-ray HRs and luminosities) are reported in Table 2 (see also Section 3.3 for more details on each source). X-ray images are presented in Appendix A with contours of the radio structures overlaid.

We detected the high-energy counterpart of two hotspots: one in the quasar 3CR 220.2 and one in 3CR 238 (see Figure 1). We discovered also X-ray emission associated with a lobe in 3CR 124 (Figure 2) and with a jet knot in the quasar

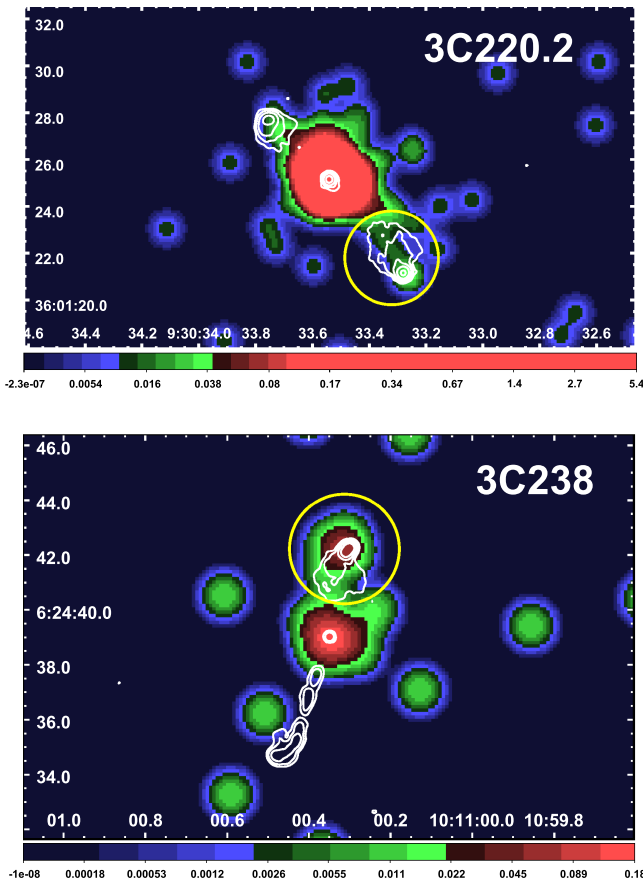


Figure 1. *Chandra* images in units of counts/pixel (bin factor of one-fourth) of 3CR 220.2 (top) and 3CR 238 (bottom) in the energy band 0.5–7 keV. Both images were smoothed with a Gaussian of FWHM = 1''. The radio contours overlaid (white), from 8.4 GHz maps, kindly supplied by C. C. Cheung, start at 0.3 mJy beam⁻¹, increasing by factors of four. The yellow circles are the regions used for the X-ray photometry of the detected hotspots.

3CR 297 (Figure 3). Detection significances, fluxes, and luminosities of the components are reported in Table 3.

Results of the X-ray spectral analysis performed for the brightest nuclei (3CR 36, 3CR 69, 3CR 119, and 3CR 220.2) are reported in Table 4: all spectra are consistent with a power-law model with Galactic absorption.

3.2. Extended Emission

In Table 2 we also listed the total number of counts within a circular region of radius 2'', N_2 , centered on the source radio nucleus. We used the radio position given in Table 1 for those sources for which the X-ray image was not registered, while for 3CR 297 we used the radio core position suggested from the flattening of the radio spectrum (see Section 3.3). As for the previous analyses of 3CR sources observed, we computed the “extent ratio,” dividing N_2 by the number of counts in a region of radius 10'', N_{10} , centered on the same position, after the subtraction of background counts measured on the CCD from both values (i.e., Ext. ratio shown in Table 2). We used the “extent ratio” as a diagnostic tool for the presence of extended X-ray emission around the source region (e.g., Massaro et al. 2009a, 2010), though it does not provide information on whether the emission is related to any extended radio structure or not. We expect values close to unity for an unresolved (i.e., point-like) source since the on-axis encircled energy for $r = 2''$ is ≈ 0.97 , so there is only a small increase between $r = 2''$ and $r = 10''$ for an unresolved source. We found

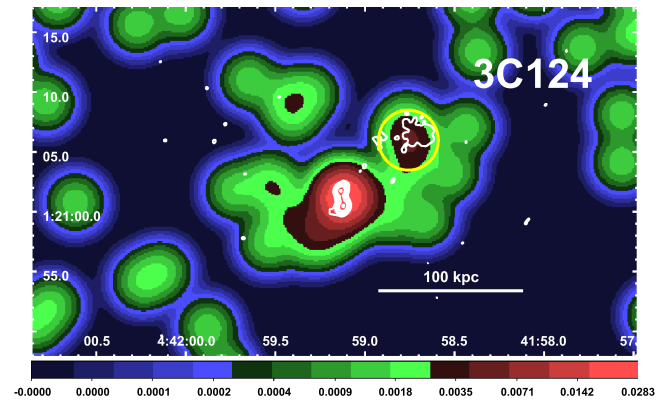


Figure 2. X-ray image of 3CR 124 in units of counts/pixel for the energy range 0.5–7 keV and bin factor one-fourth. The image was smoothed with a Gaussian of FWHM = 3''. The radio contours (white), from an 8.4 GHz map kindly provided by C. C. Cheung, start at 0.15 mJy beam⁻¹ and increase by factors of four. The NW external (relic?) lobe is detected in the X-ray and marked with the yellow circle, and the extended emission, probably arising from the hot gas in the intergalactic medium surrounding the radio source, is clearly visible in the WNW–ESE direction.

that three of the 16 sources in our sample show values of “extent ratio” less than 0.5, namely 3CR 124, 3CR 297, and 3CR 300.1, indicating the possible presence of diffuse X-ray emission. For 3CR 300.1, the indication of the presence of extended X-ray emission, given by the low value of “extent ratio,” is not reliable because its value is affected by the presence of an X-ray point source at $\sim 7''$ distance from its nucleus.

All sources showing extended X-ray emission are at $z > 1.0$, so the combination of their radio projected size, close to the limit of *Chandra* resolution, and the short exposures of snapshot observations does not always allow us to distinguish between X-ray extended emission arising from the hot intergalactic medium (IGM) in their large-scale environment and the X-ray radiation related to their large-scale radio structure (as for example IC/CMB in their radio lobes). We interpret the diffuse X-ray emission as due to the high-energy counterpart of the extended radio structure when the peaks of X-ray surface brightness appear coincident with those of the radio intensity. Otherwise we conclude that it could be due to the presence of thermal emitting gas in the IGM on a scale of several tens to hundreds of kiloparsecs. Radio images in the megahertz band, together with X-ray spectroscopic observations, are necessary to clearly disentangle the two above scenarios (Croston et al. 2005). An example is the radio galaxy 3CR 124 (see Figure 2) with an “extent ratio” of 0.49. In this source, we detected both extended X-ray emission surrounding the radio source, on the scale of tens of kiloparsecs, and X-ray diffuse emission coincident with the external lobe, asymmetrically located with respect to the main radio axis (detection significance and fluxes of the lobe are all reported in Table 3). Both emission regions contribute to the low value of “extent ratio.”

We detected X-ray emission with a brightness peak to the west side of the quasar 3CR 297 (see Figure 3). Since the radio core position of this source is unclear, radio and X-ray images are registered with the surface brightness peak position of the knot *k-w 4* (see Table 3). The presence of diffuse X-ray emission in the westward direction is not related to any radio structure, and we did not find an obvious optical counterpart in *HST* images, so we interpreted it as X-ray radiation arising from the IGM. A detailed description of this peculiar source is given in Section 3.3.

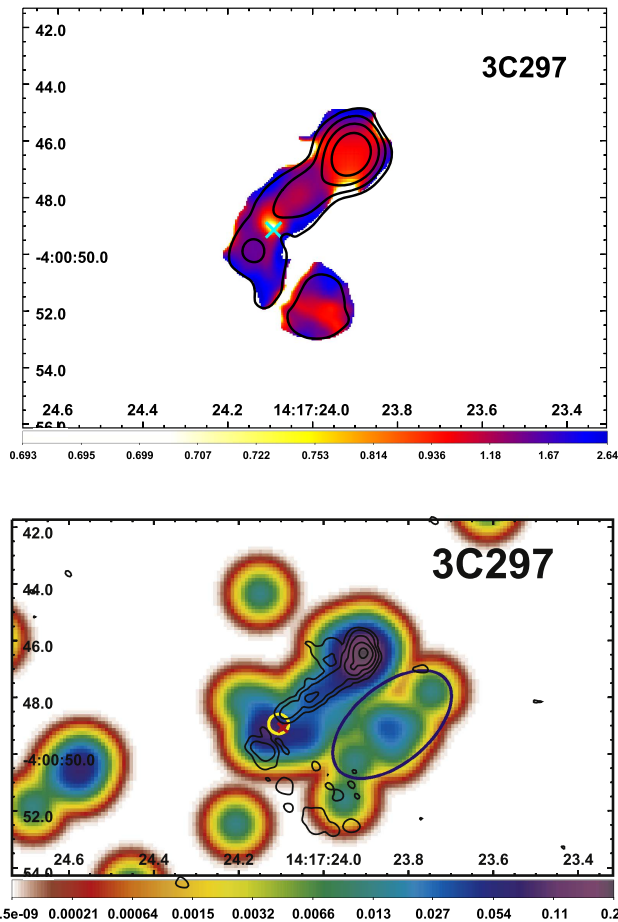


Figure 3. Top: spectral index map of 3CR 297, computed in Section 2.1, with black radio contours of the 4.9 GHz radio image superposed, starting at 2 mJy beam^{-1} and increasing by factors of four. The position of the radio core suggested from the flattening of the spectrum is marked with the cyan “ \times ” and shown also in the bottom image. Bottom: X-ray image of 3CR 297 for the energy band 0.5–7 keV and bin factor of one-fourth, in units of counts/pixel. The image was smoothed with a Gaussian of FWHM = $1''$. The black radio contours come from an 8.4 GHz map (same as in Hilbert et al. 2016) and start at $0.08 \text{ mJy beam}^{-1}$, increasing by factors of six. Since the radio core position is unclear, the two images are both registered with the surface brightness peak position of the knot *k-w* 4 (see Table 3). The position of the host galaxy in the optical *HST* observation is marked with a yellow circle, while the position of the radio core derived from the spectral index map is marked with the red “ \times .” The radio enhancement visible at $\sim 1''$ SE from the host galaxy is probably due to a field galaxy also observed in optical images, while the X-ray emission in the westward direction, marked with the blue ellipse, has no optical or radio counterparts and could arise from the hot gas in the intergalactic medium on one side of the source.

None of the 16 sources in our sample has been reported in the literature as being a member of a galaxy cluster or group, although we found that, based on the literature search reported in Section 3.3, 3CR 220.2, 3CR 255, and 3CR 300.1 could lie in large-scale (i.e., 100 kpc) galaxy-rich environments. For these sources, we searched for possible X-ray emission due to the hot gas of the intracluster medium around their radio structures (see also Massaro et al. 2018). We measured the total number of photons in a circular region containing the entire extent of the radio source, and we subtracted the X-ray counts within circular regions of $2''$, corresponding to the radio nucleus, as well as that of point-like sources (e.g., hotspots or background/foreground objects) lying within the same region. Assuming a Poisson distribution for the background events, we computed the probability of obtaining the measured value. We

did not find any X-ray excess above 3σ significance on an environment with a scale of a few hundreds of kiloparsecs.

3.3. Source Details

3CR 27 is a classical FR II radio galaxy at $z = 0.184$. From an optical perspective, it is an elliptical high-excitation radio galaxy (HERG), as confirmed by the spectrum used to update its optical identification after the last revision of the 3CR catalog (Hiltner & Röser 1991). It is located in a region of high optical obscuration at low Galactic latitude (i.e., $b = 5^\circ.5$). With the current radio map at 1.4 GHz, it was not possible to locate the radio core. However, its X-ray nucleus was probably detected with a total of 63 counts in a region of radius $\sim 2''$ centered on the celestial coordinates reported in Table 1 (Hiltner & Röser 1991) and located between the two lobes of the radio galaxy (see Figure 4). The SW hotspot has a flux density ~ 4 times greater than the northern one at 1.4 GHz. Salter & Haslam (1980) reported the detection of a possible overdensity of sources in the radio observations at 408 MHz and at 2.7 GHz over an area of $3^\circ.1 \times 1^\circ.3$ surrounding 3CR 27, without any information on its redshift. However, given the z estimate available in the literature, this corresponds to a linear size of ~ 35 Mpc, making the possible detection of a galaxy-rich environment around 3CR 27 unlikely. In addition, extended X-ray emission arising from the IGM on a scale of hundreds of kiloparsecs was not detected in our *Chandra* snapshot observation.

3CR 36 is classified as an FR II HERG at $z = 1.301$ (Hewitt & Burbidge 1991; Jackson & Rawlings 1997). In the 8.4 GHz map, its angular extension is $\sim 9''$, corresponding to a projected size of less than 80 kpc, with a dominant knotty jet in the north. In the *HST* optical image, 3CR 36 appears as a compact galaxy, and only a central nuclear component is detected (McCarthy et al. 1997). We detected the nucleus also in our *Chandra* snapshot survey (see Figure 5), and the total 335 X-ray photons observed in the nuclear region allowed us to perform a spectral analysis, which yielded a spectral index $\alpha_X = 0.7$ (see Table 4).

3CR 69 is an FR II radio galaxy, optically classified as HERG, at $z = 0.458$ (Hiltner & Röser 1991). Since the source lies in a heavily obscured region at Galactic latitude $b = -0^\circ.9$, its optical identification was made only after the last revision of the 3CR catalog. The radio image at 8.4 GHz shows two extended lobes and a fainter nucleus that was the only X-ray detection (see Figure 6). The spectral analysis of the nucleus yielded a spectral index $\alpha_X = 0.4$, as reported in Table 4, and the pileup fraction estimate is $\sim 5\%$.

3CR 119 is a CSS radio source (O’Dea 1998), and its updated redshift is $z = 1.023$ (Eracleous & Halpern 1994). The source, which in our VLA 8.4 GHz map is a compact $0''.5$ structure (~ 5 kpc at the source redshift), shows a very complex radio morphology on the 1 kpc scale observed with the VLBI at 5 GHz: the nucleus was identified with a weak, compact ($< 0''.003$) component with a flat spectrum, while the extended structure has a spiral-like form with two knots along the jet (Fanti et al. 1986). This distorted morphology was interpreted as the result of the source interaction with dense clouds in its environment, and this idea was supported by the presence of a large gradient of the rotation measure (i.e., $2300 \text{ rad m}^{-2} \text{ mas}^{-1}$ in the 8.4 GHz band) and strong depolarization between 8.4 and 5 GHz (Nan et al. 1999; Mantovani et al. 2010). The X-ray snapshot observation revealed point-like emission on a scale of $\sim 2''$, corresponding to ~ 15 kpc at the source redshift, shown in Figure 7. The spectral analysis of its nucleus yielded a value of $\alpha_X = 0.5$ (see also Table 4).

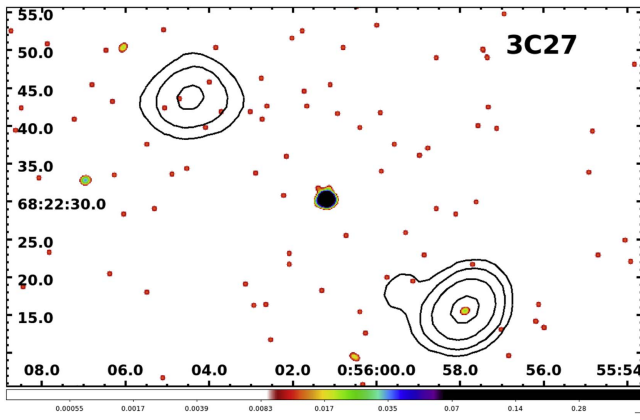


Figure 4. X-ray image of 3CR 27 for the energy band 0.5–7 keV. The image was smoothed with a Gaussian of FWHM = $1''$. The radio contours (black) come from a 1.4 GHz VLA map and start at 50 mJy beam^{-1} , increasing by factors of four. The image was not registered because of the lack of an obvious radio core, but the X-ray nuclear emission of this source was plausibly detected between the two radio lobes.

3CR 124 is an FR II radio galaxy at $z = 1.083$ (Hewitt & Burbidge 1991). Optically, it is classified as a HERG (Jackson & Rawlings 1997). The 8.4 GHz image shows a small-scale, compact double-lobe structure, with a fainter central core and angular extension of $2''$, corresponding to about 20 kpc. However, 3CR 124 also shows additional, more extended, asymmetric radio emission misaligned by $\sim 45^\circ$ measured in the W direction from the line connecting the other two, separated by $\sim 6''$ (see Figure 8), suggestive of a relic lobe (McCarthy 1989; Dunlop & Peacock 1993). The optical galaxy observed with *HST* is more extended than the radio source; it has a highly curved morphology and shows an emission-line region that is very closely aligned with the radio one (McCarthy et al. 1997; Privon et al. 2008). The two radio components aligned in the NS direction can be interpreted as the two sides of an outflow, because a velocity gradient aligned with the radio axis was measured in the form of extended [O III] $\lambda 5007$ emission regions (Shih et al. 2013).

The value of “extent ratio” computed for this source, 0.49 ± 0.09 (see Table 2), suggests the presence of diffuse emission around the nuclear region of the source. Examining the image more closely, we detect 22 photons in the $2''$ – $10''$ radial region, where we expect five background photons giving a detection of extended emission of more than 6σ . In this region, the total luminosity is $(1.1 \pm 0.2) \times 10^{44} \text{ erg s}^{-1}$.

We found an excess of X-ray photons with respect to the local background with more than 3σ level of significance in a region of radius $2''$ (see Table 3). This is spatially coincident with the lobe/relic radio emission appearing in the NE direction (see Figure 2). The local background was estimated at the same angular separation of the radio lobe/relic, thus using an annulus of $5''$ inner radius and $10''$ outer radius. However, the low number of X-ray photons does not allow us to distinguish if such emission is due to a fluctuation of the diffuse X-ray radiation that appears surrounding the nucleus also in the SE direction or due to emission arising from particles accelerated in the NE radio structure.

We could favor the latter scenario because (1) the excess of X-ray photons, spatially coincident with the NE radio structure, is ~ 2 times larger than the number of counts in the SE direction, at the same angular separation and measured over the same area, and since (2) it lies at a larger distance in the NE direction than the rest of the diffuse X-ray emission in the southern side.

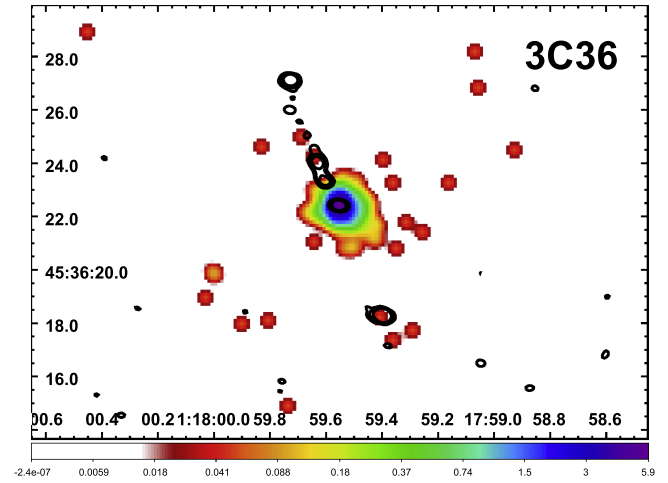


Figure 5. X-ray image of 3CR 36 for the energy band 0.5–7 keV. The image was smoothed with a Gaussian of FWHM = $0''$. The radio contours (black) come from an 8.4 GHz VLA map and start at 1 mJy beam^{-1} , increasing by factors of four.

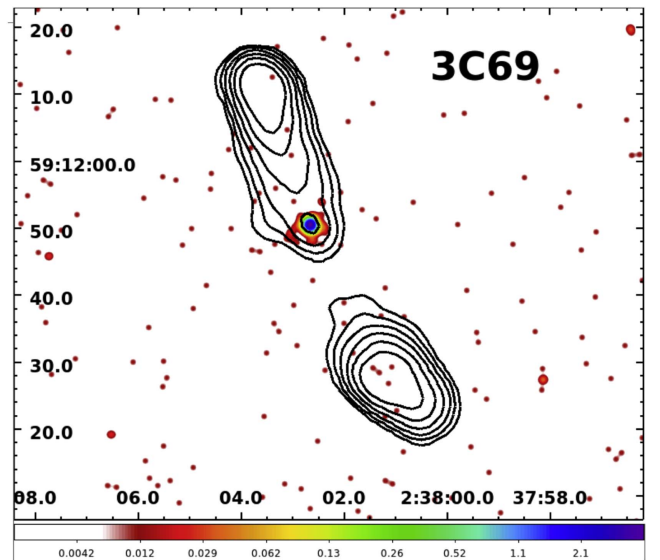


Figure 6. X-ray image of 3CR 69 for the energy band 0.5–7 keV. The *Chandra* image was smoothed with a Gaussian of FWHM = $1''$. The radio contours (black) come from a 4.9 GHz VLA map and start at 2 mJy beam^{-1} , increasing by factors of two.

Nuclear X-ray emission was also detected by *Chandra* (see Figure 8).

3CR 173 is a CSS at $z = 1.035$, optically classified as a HERG (Jackson & Rawlings 1997). A double structure is visible in the radio image at 4.9 GHz, with the two peaks of radio surface brightness separated by only $\sim 2''$, corresponding to ~ 15 kpc at the source redshift (see Figure 9). The core is the dominant SW component, characterized by a flattening of the integrated radio spectrum near 38 MHz (Tyul’bashev & Chernikov 2000), and it is the only X-ray detection in this source.

3CR 194, at $z = 1.184$ (Strom et al. 1990), was optically classified as a HERG (Jackson & Rawlings 1997), and it is an FR II radio galaxy with a double hotspot in the NW lobe (see Figure 10). A high-sensitivity VLA image at 8.4 GHz showed that the two radio lobes are asymmetrically located with respect to the radio core, and the northwestern lobe does not extend along the radio source axis, but is almost perpendicular to it

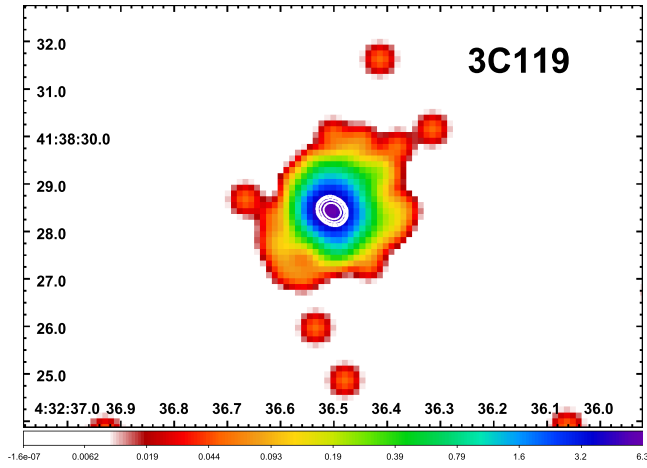


Figure 7. X-ray image of 3CR 119 for the energy band 0.5–7 keV. The image was smoothed with a Gaussian of $\text{FWHM} = 0''.5$. The radio contours (white) come from an 8.4 GHz VLA map and start at 10 mJy beam^{-1} , increasing by factors of four.

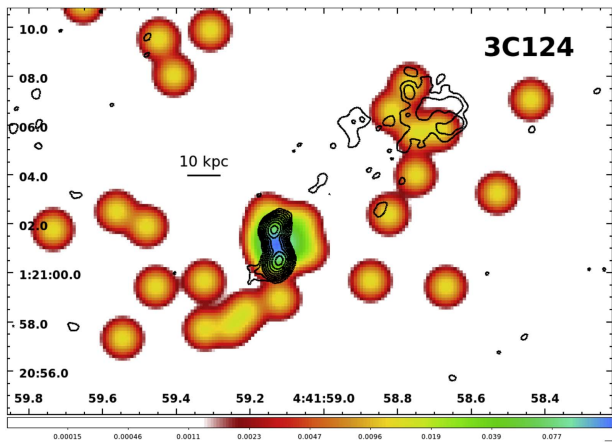


Figure 8. X-ray image of 3CR 124 for the energy band 0.5–7 keV. The image was smoothed with a Gaussian of $\text{FWHM} = 1''.0$. The radio contours (black) come from a 8.4 GHz map, kindly provided by C. C. Cheung, and start at $0.12 \text{ mJy beam}^{-1}$, increasing by factors of two. The NW external lobe is detected with five counts in the X-ray, and diffuse extended emission is observed on a 100 kpc scale in the WNW–ESE direction.

(Fermi 2014). Weak radio emission in the EW direction was also observed at 5 GHz, giving an irregular quadrupolar shape and suggesting a movement of the source in the ambient medium in a westward direction (Strom et al. 1990). The optical galaxy in *HST* images is elongated NS and is composed of two components separated by $2''$ (Djorgovski et al. 1988; McCarthy et al. 1997). 3CR 194 displays rotation measures (in high-resolution VLA observations at 1.4, 4.9, and 8.4 GHz) in excess of 1000 rad m^{-2} with an enhancement coincident with the NW hotspot (Taylor et al. 1992): the excess was interpreted as being due to the compression of external gas and magnetic field by the terminal shock that created the hotspot. This suggests the presence of high-density, hot gas surrounding the galaxy, however lacking an X-ray detection. With 124 counts, the X-ray emission of the nuclear region of this galaxy was clearly observed by *Chandra*.

3CR 208.1 is a quasar (QSO). The optical counterpart was first identified with an N-type galaxy at $z = 1.02$ (Spinrad et al. 1985). Gravitational amplification due to a foreground source $\sim 3''$ SE at $z = 0.159$ was found to brighten the QSO by

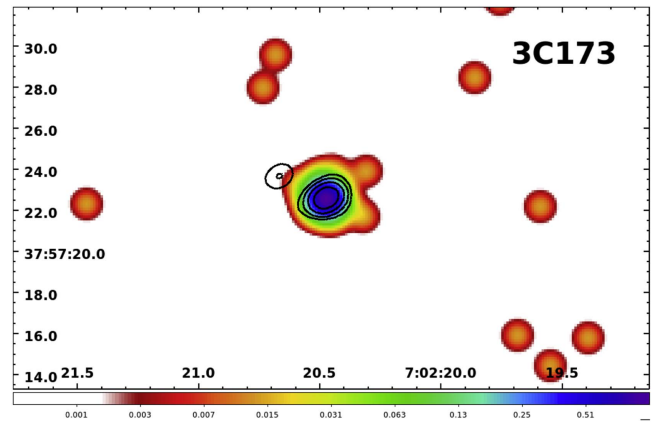


Figure 9. X-ray image of 3CR 173 for the energy band 0.5–7 keV. The image was smoothed with a Gaussian of $\text{FWHM} = 1''.0$. The radio contours (black) come from a 4.9 GHz VLA map and start at 25 mJy beam^{-1} , increasing by factors of two.

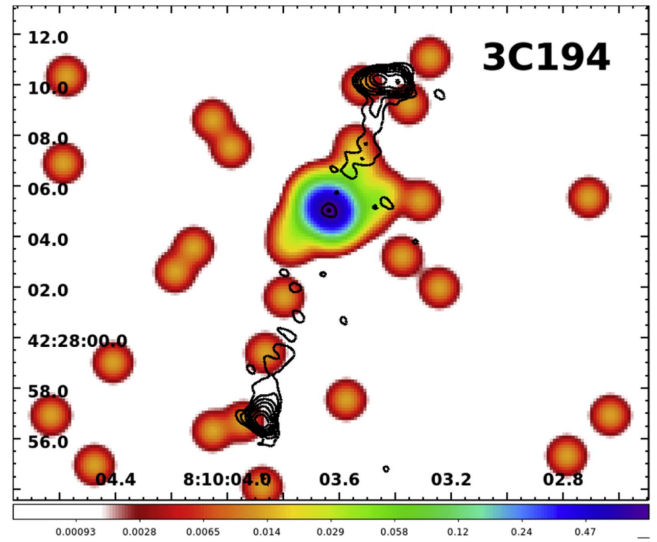


Figure 10. X-ray image of 3CR 194 for the energy band 0.5–7 keV. The image was smoothed with a Gaussian of $\text{FWHM} = 1''.0$. The radio contours (black) come from a 4.9 GHz VLA map and start at $1.4 \text{ mJy beam}^{-1}$, increasing by factors of two.

several tenths of a magnitude and to increase its radio flux by a factor of 1.5 (Le Fèvre & Hammer 1990). The optical image of 3CR 208.1 has a compact nucleus and a secondary component $0''.6$ NE (McCarthy et al. 1997), while the radio image at 14.9 GHz shows a lobe $5''$ NW with a curved jet. The only feature detected by *Chandra* is the radio core (see Figure 11).

3CR 220.2 is a QSO at $z = 1.157$ (Spinrad et al. 1985). In the radio image at 4.9 GHz, both lobes, separated by ~ 60 kpc, show a hotspot in the outer region. The peak of the radio surface brightness in the southern hotspot is coincident with a feature visible in the *HST* optical image, but also with the peak of the X-ray emission detected and designated as *h-s5* in Table 3. Two X-ray photons are detected in the radio NE lobe/hotspot region. However, given the presence of X-ray photons at similar angular separation from the radio core with no radio counterparts, we cannot exclude that those in the northern lobe/hotspot are fluctuations of the local background. The X-ray nuclear emission is consistent with an unresolved point source, despite the presence of an elongation of the X-ray emission along the radio axis visible in Figures 1 and 12.

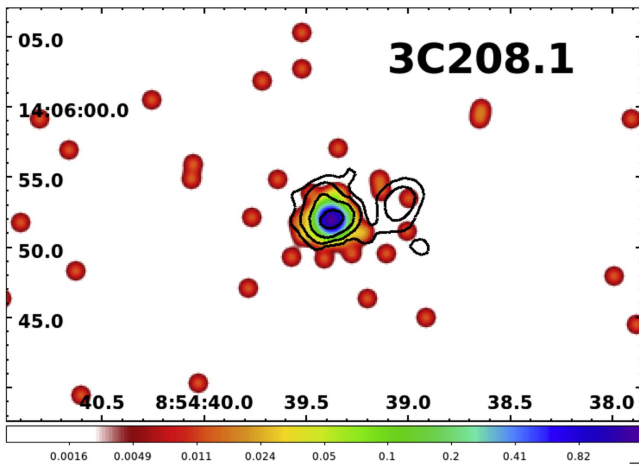


Figure 11. X-ray image of 3CR 208.1 for the energy band 0.5–7 keV. The *Chandra* image was smoothed with a Gaussian of FWHM = 1''. Radio contours (black) come from a 14.9 GHz VLA map and start at 1.5 mJy beam⁻¹, increasing by factors of four.

In IR and optical images, the source is aligned with a group of large spiral galaxies (Hilbert et al. 2016). Based on the photometric redshift estimations of the Sloan Digital Sky Survey (Albareti et al. 2017), these objects are probably foreground galaxies. However, we searched for extended X-ray emission on a scale of hundreds of kiloparsecs in the field of 3CR 220.2 and found no neat detection.

The nucleus of 3CR 220.2 is the brightest one within the sample (i.e., $N_2 = 683$), and it has a spectral index $\alpha_X = 0.6$ (see Table 4). The pileup fraction obtained for this source is $\sim 8.5\%$, but the spectral index obtained using a pileup model (i.e., $\alpha_X = 0.81_{-0.25}^{+0.08}$) is consistent with 0.6.

3CR 222 is known to be the most distant FR I radio galaxy of the 3CR catalog to date, having $z = 1.339$ (Heckman et al. 1994), although there is no published spectrum in the literature. It was classified as an ultrastep-spectrum radio source, since it has a radio spectral index $\alpha_R = 1.52$ in the frequency range from 10 MHz to 1 GHz (Roland et al. 1982). 3CR 222 was described as a compact double radio source, dominated by the nuclear emission at 1.4 GHz and with steep-spectrum emission coming from a region separated by 1''.2 to the south (Strom et al. 1990; Law-Green et al. 1995). The optical identification is the western member of an apparent faint quartet (Djorgovski et al. 1988). The X-ray nucleus is detected at 3σ level of significance with only three photons observed by *Chandra* in a circular region of radius 2'' (see Figure 13).

3CR 230 is an FR II radio galaxy at $z = 1.487$ with a double hotspot at the end of the northern lobe (Hewitt & Burbidge 1991). It is optically classified as a HERG (Jackson & Rawlings 1997). The radio image at 8.4 GHz shows two knots along the southern jet: it was claimed that the radio core position is coincident with the northern one, at R.A. = 9^h51^m58^s.90 and $\delta = -00^{\circ}01'27''.87$ (J2000.0; Steinbring 2011). However, a comparison with the *HST* (Hilbert et al. 2016) and *WISE* (Wright et al. 2010) images of the sources shows that the optical nucleus is 0''.5 N of this position. Moreover, since the shift that should be applied to register the X-ray image with the radio core identified by Steinbring is $\sim 1''.5$, more than twice the average shift imposed on the other sources, we used the unregistered image (see Figure 14).

By studying the relationship between source outflow and star formation in this galaxy, Steinbring noticed that the asymmetry of the 3CR 230 radio structure is mirrored in the optical surface

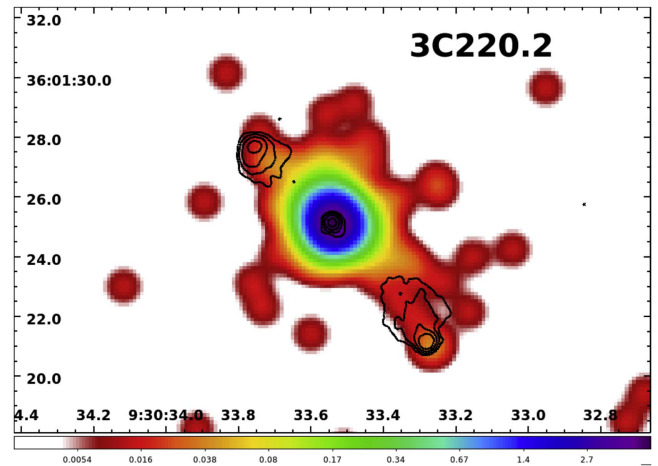


Figure 12. X-ray image of 3CR 220.2 for the energy band 0.5–7 keV. The image was smoothed with a Gaussian of FWHM = 1''. The radio contours (black) come from a 8.4 GHz map, kindly supplied by C. C. Cheung, and start at 0.3 mJy beam⁻¹, increasing by factors of four. The nucleus and the SW hotspot are detected in the X-ray. An elongation of the X-ray emission is observed along the lobe axis, but, within 3'', the source is statistically consistent with the PSF.

brightness and in the strong turbulence in the direction of the shorter radio arm to the SW. The optical galaxy runs along a central spine SE to NW aligned with the radio lobes and ends in broader tails, while the observed linear structures due to star formation are possibly induced by the jet (Hilbert et al. 2016). 3CR 230 is identified as a possible cluster candidate according to the red sequence method (Kotyla et al. 2016). The nucleus is the only X-ray detection, although its position is uncertain.

3CR 238 is a HERG with a classical FR II morphology at $z = 1.405$ (Jackson & Rawlings 1997). It could be affected by gravitational lensing by the Abell cluster A949 with an estimated redshift $z = 0.142$ along its line of sight (Le Fèvre et al. 1988). However, the core of this galaxy cluster is outside the field of view of the *Chandra* observation. The optical observation made with the *HST* shows a compact nucleus and faint extensions in the NS direction (McCarthy et al. 1997). In the 8.4 GHz image, the southern jet shows two elongated knots separated by 1'' and 2'' from the nucleus, while the northern knot has a wider structure that is also detected in the X-ray (see Table 3 and Figure 1). The offset of $\sim 0''.2$ between the peak of X-ray and radio emission is within the *Chandra* position error (see, e.g., Massaro et al. 2011). We also checked the *HST* field, and we did not find any optical source that could be associated with this X-ray emission. The “extent ratio” value computed for this source, as reported in Table 2, is < 0.9 , and it indicates the presence of extended emission ascribed to the X-ray radiation associated with the hotspot (see Figure 15).

3CR 255 is a $z = 1.355$ radio galaxy with two radio components separated by 10 kpc (Giraud 1990). It is optically classified as a HERG (Jackson & Rawlings 1997). The 8.4 GHz map indicates a weak signal at the center of the host galaxy, as well as a brighter, compact radio source to the SE (see Figure 16). The northern radio component is located at the position of the optical galaxy, but more data are necessary to verify if it is compact and if it has a flat radio spectrum, as expected for the core of radio galaxies. In the optical band, the source appears elongated on a 1'' scale, and an overdensity of objects with optical magnitude in the R band between 22.5 and 24 was found in a 62'' \times 62'' area around the target (Giraud 1991). This suggests the presence of a group or cluster of galaxies on the scale of

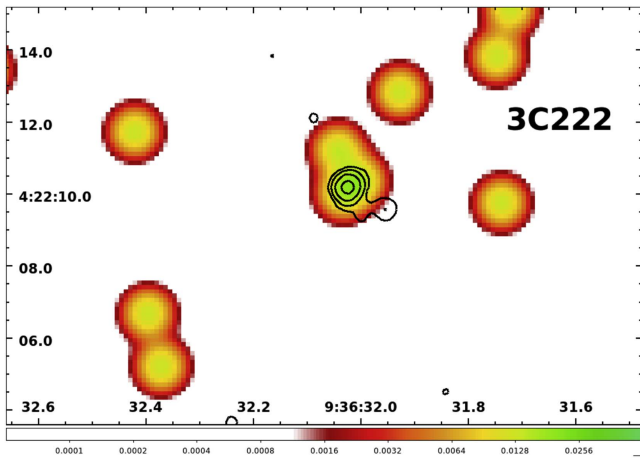


Figure 13. X-ray image of 3CR 222 for the energy band 0.5–7 keV. The *Chandra* image was smoothed with a Gaussian of $\text{FWHM} = 1''.0$. The radio contours (black) come from a 4.9 GHz VLA map and start at 1 mJy beam^{-1} , increasing by factors of four.

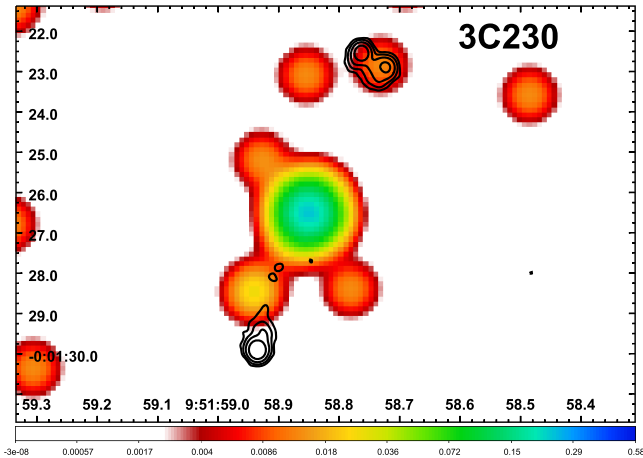


Figure 14. X-ray image of 3CR 230 for the energy band 0.5–7 keV. The image was smoothed with a Gaussian of $\text{FWHM} = 1''.0$. The radio contours (black) come from an 8.4 GHz map, kindly provided by C. C. Cheung, and start at $0.3 \text{ mJy beam}^{-1}$, increasing by factors of four. The X-ray image has not been registered because the radio core position is uncertain.

~ 500 kpc. An IR *HST* image with $\sim 0''.1$ resolution shows several extended sources in the vicinity of 3CR 255 (Hilbert et al. 2016). In the NASA/IPAC Extragalactic Database, these objects are all cataloged as infrared sources with no redshift estimation. All of them have a clear optical counterpart, suggesting that active star formation is ongoing (Hilbert et al. 2016). The possible suggestion of the presence of a small group of galaxies in the field of 3CR 255 comes also from the red sequence method (Kotyla et al. 2016). However, we did not detect extended X-ray emission in the hundreds of kiloparsecs environment of this source. 3CR 255 lies entirely in a region of $2''$ radius in which *Chandra* observed only five X-ray photons.

3CR 297 is a quasar with a peculiar radio morphology, lying at $z = 1.406$ (Spinrad et al. 1985). The emission observed in the 8.4 and 4.85 GHz maps, computed in Section 2.1, is elongated and curved with a knotty enhancement at the end of the northern jet (see Figure 3). In both radio images, the emission to the south spreads over a much wider area, with a stronger concentration of signal centered on a double elongated source approximately 8 kpc (i.e., $\sim 1''$) in projected distance from the host galaxy. The optical image shows two components separated by $0''.3$ (McCarthy

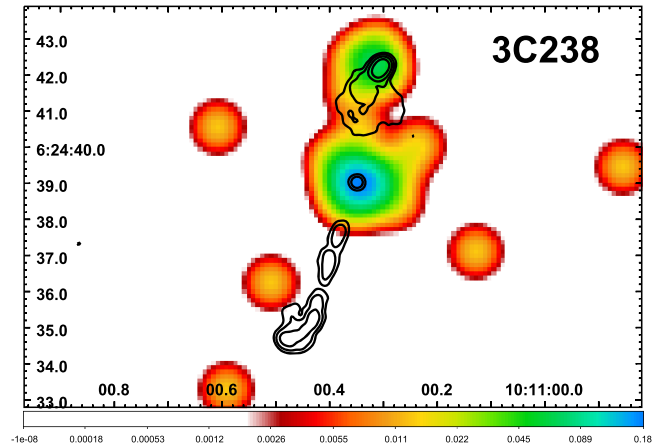


Figure 15. X-ray image of 3CR 238 for the energy band 0.5–7 keV. The image was smoothed with a Gaussian of $\text{FWHM} = 1''.0$. The radio contours (black) come from an 8.4 GHz map, kindly supplied by C. C. Cheung, and start at $0.3 \text{ mJy beam}^{-1}$, increasing by factors of four. The northern hotspot and the nucleus are detected in the X-ray.

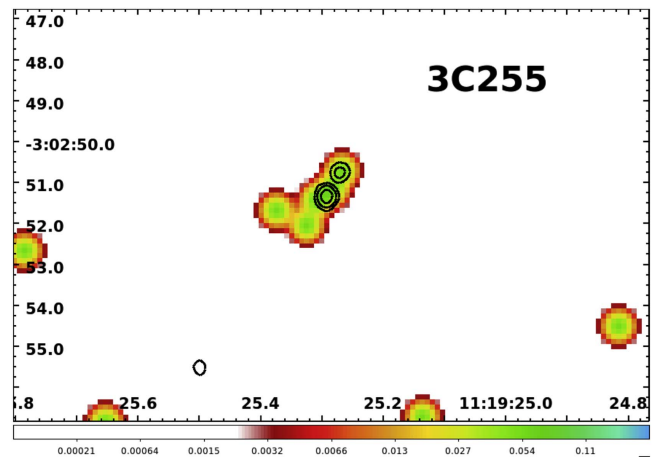


Figure 16. X-ray image of 3CR 255 for the energy band 0.5–7 keV. The image was smoothed with a Gaussian of $\text{FWHM} = 0''.5$. The radio contours (black) come from a 8.4 GHz VLA map and start at 1 mJy beam^{-1} , increasing by factors of four.

et al. 1997). Recent *HST* IR and optical images suggest the presence of ongoing merger activity in the area (Hilbert et al. 2016).

X-ray emission surrounding the radio jet is extended, and there are 33 X-ray photons coincident with the position of the peak of the radio intensity of the jet knot in the NW (see Figure 17). Its detection, X-ray fluxes, and luminosity are reported in Table 3. The precise location of the 3CR 297 nucleus in the radio maps available to us was uncertain, so we decided to perform the astrometric registration using the radio position of the jet knot (i.e., $\text{R.A.} = 14^{\text{h}}17^{\text{m}}23^{\text{s}}905$, $\delta = -04^{\circ}00^{\text{m}}46^{\text{s}}42$, J2000.0), assuming that the peak of X-ray surface brightness coincides with the radio peak. We then estimated the radio core position, indicated by the flattening of the radio power-law spectrum, using the spectral index map computed in Section 2.1. As shown in Figure 3, the minimum value of spectral index, $\alpha_R = 0.68$, is reached at $\text{R.A.} = 14^{\text{h}}17^{\text{m}}24^{\text{s}}095$, $\delta = -04^{\circ}00^{\text{m}}49^{\text{s}}06$ (J2000.0), almost coincident with the optical host galaxy. We used also the *HST* observation to compare the morphology of the source in the radio, X-ray, and optical bands.

X-ray diffuse emission was observed in a $2'' \times 4''$ region west of the source with six X-ray counts and a total luminosity

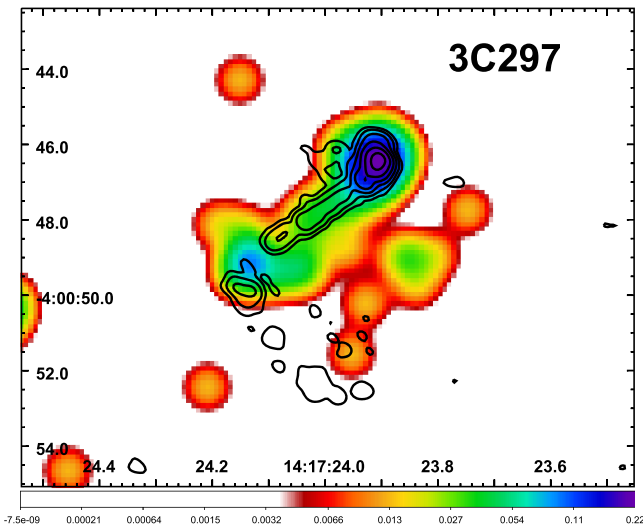


Figure 17. X-ray image of 3CR 297 for the energy band 0.5–7 keV. The image was smoothed with a Gaussian of $\text{FWHM} = 1''$. The radio contours (black) come from a 8.4 GHz VLA map (Hilbert et al. 2016) and start at $0.08 \text{ mJy beam}^{-1}$, increasing by factors of four. The image is registered with the NW knot position. The nucleus is detected in the X-ray, although its position is uncertain. The X-ray emission in the westward direction has no optical or radio counterpart.

of $(6 \pm 2) \times 10^{43} \text{ erg s}^{-1}$: since no optical counterpart was found in the *HST* image, this emission could be due to hot gas in the large-scale environment.

3CR 300.1 is a classical FR II HERG at $z = 1.159$ (Djorgovski et al. 1988), with two lobes separated by $\sim 10''$ (i.e., $\sim 80 \text{ kpc}$ at the source redshift) and a central core fainter than the lobes in the 14.9 GHz map (Jackson & Rawlings 1997). The radio core is not detected in the 8.4 GHz radio image. In *HST* IR images, the galaxy appears as an extended irregular source with diffuse emission that suggests the presence of active star-formation regions (Hilbert et al. 2016).

Kotyla et al. (2016) reported a possible presence of a source overdensity surrounding 3CR 300.1 and a possible cluster/group detection using the “red sequence” method that does not appear clearly evident to us, but we checked for the presence of diffuse X-ray emission on the tens of kiloparsecs scale in our *Chandra* snapshot observation. At a projected distance of $\sim 7''$ in the SW direction, we detected an X-ray point source that has an IR counterpart in an *HST* image (see Figure 18). The value of “extent ratio” computed in Table 2 indicates the presence of extended emission around its nucleus, but we did not find a relevant detection in the annular region surrounding the radio source, if we exclude the background/foreground source.

The two radio lobes are detected with more than 2σ level of significance using a local background. This was estimated in an annulus of $3''$ inner radius and $8''$ outer radius.

3CR 305.1 at $z = 1.132$ (Spinrad et al. 1985) is cataloged as a CSS (O’Dea 1998), and optically it is the only low-excitation radio galaxy (LERG) in our sample. The optical galaxy has a complex morphology suggestive of ongoing merger activity (Hilbert et al. 2016): the optical emission can be seen over more than $2''$ with a curved S-shaped structure in the inner $1''$ radius and a close agreement between optical and radio orientation (McCarthy et al. 1997). Radio images at 8.4 GHz show the northern jet with more elongated emission and a southern circular lobe. In the 15 GHz radio map, the northern jet shows three knots. The southernmost has a radio spectral index of 0.6 and is highly

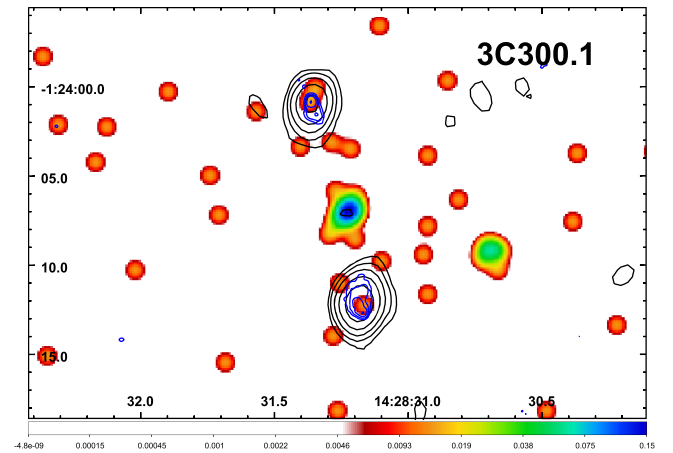


Figure 18. X-ray image of 3CR 300.1 for the energy band 0.5–7 keV. The *Chandra* image was smoothed with a Gaussian of $\text{FWHM} = 1''$. The black radio contours come from a 14.9 GHz VLA map and start at $3.5 \text{ mJy beam}^{-1}$, increasing by factors of two; the blue ones come from an 8.4 GHz map and start at $0.6 \text{ mJy beam}^{-1}$, increasing by factors of four. The radio core is visible only in the 14.9 GHz map and is X-ray detected, while, $\sim 7''$ SW from the nucleus, there is a point-like X-ray field source.

polarized (60%), so it is unlikely to be the core (van Breugel et al. 1992). No nuclear emission is detectable in the radio maps available to us, ranging from 1.5 to 22.5 GHz. Thus the registration was not performed. This source is detected with 16 X-ray photons in our *Chandra* image (see Figure 19).

4. Summary and Conclusions

We presented new *Chandra* X-ray observations of 16 radio sources listed in the Third Cambridge Revised catalog, observed during *Chandra* Cycle 17. The current sample lists three compact steep spectrum sources, three quasars, nine FR II radio galaxies, and the most distant FR I radio galaxy within the 3CR extragalactic catalog. Fourteen targets lie at z in the range 1.0–1.5, plus 3CR 27 and 3CR 69, which lie at $z = 0.184$ and $z = 0.458$, respectively.

Thanks to the *Chandra* snapshot survey, all 3CR extragalactic sources with $z < 1.5$ have at least an exploratory X-ray observation available to the astronomical community, enabling us to (1) search for X-ray emission from jet knots, hotspots, and lobes in radio sources; and (2) investigate the high-energy emission arising from the IGM in the environments of quasars and radio galaxies, at different scales.

Here, the basic source parameters for the newly acquired data are presented. We built flux maps for all of the X-ray observations in three energy ranges (0.5–1 keV, 1–2 keV, and 2–7 keV), and we provide basic parameters, including net counts, fluxes, and luminosity, for the nuclei and other radio structures detected (i.e., jet knots, hotspots, lobes). In addition, we performed X-ray spectral analysis of the four brightest nuclei, finding consistency with a simple power-law spectrum with Galactic absorption.

The three CSS radio sources in our sample appear as point-like X-ray sources (see O’Dea et al. 2017 for a recent discussion of X-ray observations of CSS radio sources).

We discovered the X-ray counterparts of two radio hotspots (one in 3CR 220.2 and the other in 3CR 238) and of a lobe or relic in 3CR 124. Moreover, we discovered extended X-ray emission around the nuclear regions of 3CR 124 and 3CR 297 on the scale of $\sim 10''$ and $\sim 5''$, corresponding to 85 and 45 kpc, respectively. In the quasar 3CR 297, we discovered diffuse

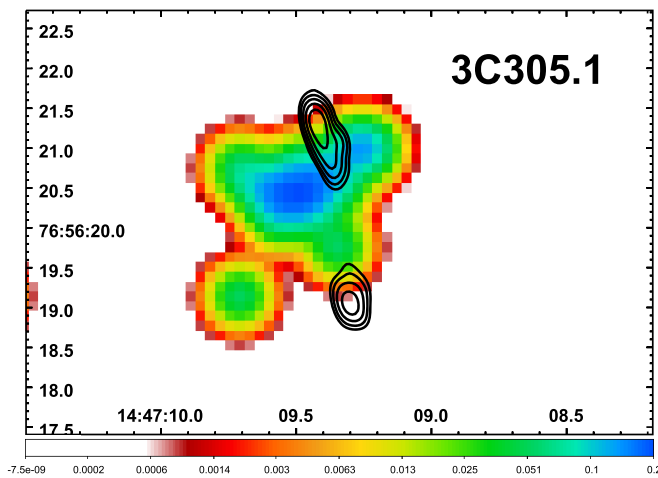


Figure 19. X-ray image of 3CR 305.1 for the energy band 0.5–7 keV. The image was smoothed with a Gaussian of FWHM = $0''.5$. The radio contours (black) come from an 8.4 GHz VLA map and start at 2 mJy beam^{-1} , increasing by factors of two. No astrometric registration was performed for this source.

X-ray emission, of still unknown nature, along and parallel to the main radio axis.

Finally, a table summarizing the state of the art of the X-ray (i.e., *Chandra* and *XMM-Newton*) observations of 3CR extragalactic sources carried out to date is also reported at the end of the present manuscript (see Appendix B). *Chandra* detections are based on both our previous and current analyses and represent an update with respect to previous works, while those regarding *XMM-Newton* are only based on the literature search carried out to date.

We thank the anonymous referee for useful comments that led to improvements in the paper. We are grateful to C. C. Cheung for providing several radio images of the 3CR sources,²¹ while the remaining ones were downloaded from NVAS²² (NRAO VLA Archive Survey), NED²³ (NASA/IPAC Extragalactic Database), and the DRAGN web page.²⁴ This investigation is supported by National Aeronautics and Space Administration (NASA) grants GO4-15097X, GO4-15096X, GO6-17081X, and AR6-17012X. G.R.T. acknowledges support from NASA through the Einstein Postdoctoral Fellowship Award Number PF-150128, issued by the *Chandra* X-ray Center, which is operated by the Smithsonian Astrophysical Observatory (SAO) for and on behalf of NASA under contract NAS8-03060. The National Radio Astronomy Observatory is operated by Associated Universities, Inc., under contract with the National Science Foundation. This research has made use of data obtained from the High-Energy Astrophysics Science Archive Research Center (HEASARC) provided by NASA’s Goddard Space Flight Center; the SIMBAD database operated at CDS, Strasbourg, France; and the NED operated by the Jet Propulsion Laboratory, California Institute of Technology, under contract with NASA. TOPCAT²⁵ (Taylor 2005) and SAOImage DS9, developed by the SAO, were extensively used in this work for the preparation and manipulation of the tabular data and images.

Facilities: VLA, CXO (ACIS).

²¹ <http://www.slac.stanford.edu/~teddy/vla3cr/vla3cr.html>

²² <http://archive.nrao.edu/nvas/>

²³ <http://ned.ipac.caltech.edu/>

²⁴ <http://www.jb.man.ac.uk/atlas/>

²⁵ <http://www.star.bris.ac.uk/~mbt/topcat/>

Appendix A Images of the Sources

Although for many radio sources in our sample the X-ray data are detected with rather few counts, the radio morphologies are shown here via contour diagrams that are superposed on X-ray images. The *Chandra* images shown are in units of counts/pixel in the 0.5–7 keV energy range. All of the X-ray images were regridded with a bin factor one-fourth to obtain a common pixel size of $0''.123$, and then smoothed with a Gaussian function. The FWHM of the Gaussian smoothing function is given in the figure captions, as well as the increasing factors of the radio contours overlaid. Figures appear different from each other because of the wide range in angular size of the radio sources, and it is worth noting that 3CR 27 and 3CR 69 are in a different redshift range than the other sources.

Appendix B X-Ray Observations of the 3CR Sample

In Table 5 we list the summary of the X-ray observations for the 3CR extragalactic sample carried out with *Chandra* and *XMM-Newton*.

Chandra X-ray observations have been uniformly analyzed, as reported in our previous and current investigations, as part of the *Chandra* 3CR survey project. The 3CR extragalactic portion of the catalog includes 298 sources (Spinrad et al. 1985). Adopting a step-wise strategy, we requested the observation of small subsamples in each cycle, to minimize the impact on the *Chandra* schedule. The full observational coverage of all 3CR sources with $z < 0.3$ was achieved during *Chandra* Cycles 9 and 12, for a total of 56 sources observed (Massaro et al. 2010, 2012). An additional 19 3CR radio galaxies were published in 2013 ($0.3 < z < 0.5$, *Chandra* Cycle 13, in Massaro et al. 2013), and a data paper presenting the most recent observations of 23 sources was accepted in 2017 ($0.5 < z < 1.0$, Cycle 15, in Massaro et al. 2018). We also performed a uniform reanalysis of 140 objects, listed in the *Chandra* archive, adopting the same data reduction procedures, from which we excluded seven sources that have been extensively discussed in the literature and three other sources for Principal Investigator reasons (Massaro et al. 2011, 2015 and references therein). Several subsets of the 3CR sample have been also observed by other groups (e.g., Balmaverde et al. 2012; Wilkes et al. 2013). Here we present an update of the summary also including the 16 targets analyzed in the present work (Cycle 17).

Of the remaining 34 sources unobserved by *Chandra*, 25 are still unidentified, lacking an assigned optical/IR counterpart. We recently observed 21 of these 25 targets with *Swift* snapshot observations, discovering X-ray counterparts of 11 of them, but even using optical and ultraviolet data available from the instruments on board the *Swift* satellite, we could not discern their optical counterparts (Maselli et al. 2016).

The *XMM-Newton* archive covers to date $\sim 35\%$ of the entire 3CR extragalactic catalog, and all of the information provided here is only based on a literature search (see, e.g., Croston et al. 2005, 2008; Evans et al. 2006; Belsole et al. 2007; Laskar et al. 2010; Shelton et al. 2011; Ineson et al. 2013, 2017; Mannering et al. 2013, and references therein for more details).

We report the 3CR name, the updated value of the redshift z , and the radio classification of each source, labeling as follows: radio galaxies (RG), according to the Fanaroff & Riley criterion (Fanaroff & Riley 1974); quasars (QSO); Seyfert galaxies (Sy);

and BL Lac objects (BL). We indicate as “UNID” those sources lacking a clear optical/IR counterpart. Then we also added a column reporting the radio morphology for the radio galaxies (FR I versus FR II classes) and indicating those objects that also show the radio structure of (1) compact steep spectrum (CSS) or X-shaped (XS) radio sources or (2) have been classified in the literature as wide-angle tailed or narrow-angle tailed radio galaxies (WAT and NAT, respectively). We devoted a column to the optical classification of radio galaxies distinguishing between HERG or LERG. We used a “cluster flag” to label sources for which there is an associated optical group/cluster reported in the literature or those for which an archival X-ray observation confirms the presence of hot gas in the intracluster medium.

For what concerns the X-ray, we verified the presence of *Chandra* or *XMM-Newton* observations, indicating with different symbols if the source was already observed by *Chandra* (c) or *XMM-Newton* (x). We report X-ray detections of radio components, that is, jet knot, hotspot, or lobe, with the symbols *k*, *h*, and *l*, respectively. The symbol *igm* was used to indicate the detection of X-ray-emitting IGM. For *Chandra* observations, we also adopted the symbol *e* for the sources that show extended X-ray emission around the nucleus highlighted in our analyses by the “extent ratio” measurements (see Section 3.2). For *XMM-Newton* observations, we only adopted the *l* and *igm* labels due to the lower angular resolution with respect to *Chandra* that does not allow us to see counterparts of jet knots and hotspots in a large fraction of the 3CR sources.

Table 5
Summary of the 3CR X-Ray Observations

3CR ^a name	z ^b	Class ^c	Radio ^d morph.	Optical ^e class	Cluster ^f flag	X-Ray ^g obs.	<i>Chandra</i> ^h detections	<i>XMM-Newton</i> ⁱ detections
2.0	1.037	QSO				c	e	
6.1	0.840	RG	FR II	HERG		c	h	
9.0	2.020	QSO	LDQ			c	k;l	
11.1	?	UNID		x		
13.0	1.351	RG	FR II	HERG		c-x	e;h	
14.0	1.469	QSO				c		
14.1	?	UNID		x		
15.0	0.074	RG	FR I	LERG		c	k;l	
16.0	0.405	RG	FR II	HERG		c-x	e;h;l	
17.0	0.220	QSO				c	k	
18.0	0.188	RG	FR II	HERG		c	e	
19.0	0.482	RG	FR II	LERG	✓	c-x	h;igm	
20.0	0.174	RG	FR II	HERG		c-x		
21.1	?	UNID	...	-		x		
22.0	0.936	RG	FR II			c		
27.0	0.184	RG	FR II	HERG		c		
28.0	0.195	RG	FR I	LERG	✓	c-x	igm	igm
29.0	0.045	RG	FR I	LERG	✓	c	k;igm	
31.0	0.017	RG	FR I	LERG	✓	c-x	k	igm
33.0	0.060	RG	FR II	HERG	✓	c-x	h;l	l;igm
33.1	0.181	RG	FR II	HERG		c		
33.2	?	UNID		x		
34.0	0.69	RG	FR II	HERG	✓	c	igm	
35.0	0.067	RG	FR II	LERG	✓	c-x	e;l	l;igm
36.0	1.301	RG	FR II	HERG		c		
40.0	0.018	RG	FR I-WAT	LERG	✓	c-x	igm	igm
41.0	0.795	RG	FR II	HERG		c	h	
42.0	0.396	RG	FR II	HERG		c-x		
43.0	1.459	QSO	CSS			c		
44.0	0.66	QSO			✓	c		
46.0	0.437	RG	FR II	HERG	✓	c-x		igm
47.0	0.425	QSO	LDQ			c	h;l	
48.0	0.367	QSO	CSS			c		
49.0	0.236	RG	FR II-CSS	HERG		c		
52.0	0.29	RG	FR II-XS	HERG	✓	c	h	
54.0	0.827	RG	FR II	HERG		c	h	
55.0	0.735	RG	FR II	HERG		c-x		
61.1	0.188	RG	FR II	HERG		c-x	h	
63.0	0.175	RG	FR II-XS	HERG		c		
65.0	1.176	RG	FR II	HERG		c-x	e;h	
66A	?	BL	✓	c-x		
66B	0.0213	RG	FR I	LERG	✓	c-x	k	igm
67.0	0.310	RG	FR II-CSS			c-x		
68.1	1.238	QSO				c		
68.2	1.575	RG	FR II	HERG		c	e;h	
69.0	0.458	RG	FR II	HERG		c		
71.0	0.004	SEY	...	Sy2		c-x		

Table 5
(Continued)

3CR ^a name	z^b	Class ^c	Radio ^d morph.	Optical ^e class	Cluster ^f flag	X-Ray ^g obs.	<i>Chandra</i> ^h detections	<i>XMM-Newton</i> ⁱ detections
75.0	0.023	RG	FRI-WAT	LERG	✓	c-x	igm	igm
76.1	0.032	RG	FRI	LERG	✓	c-x	igm	igm
78.0	0.029	RG	FRI	LERG		c	k	
79.0	0.256	RG	FRII	HERG	✓	c-x		igm
83.1	0.025	RG	FRI-NAT	LERG	✓	c-x	k;igm	igm
84.0	0.018	RG	FRI	LERG	✓	c-x	igm	igm
86.0	?	UNID				
88.0	0.030	RG	FRI	LERG	✓	c-x	k;igm	igm
89.0	0.140	RG	FRI-WAT	LERG	✓	c	igm	
91.0	?	UNID				
93.0	0.357	QSO				c	e	
93.1	0.243	RG	FRII-CSS	HERG	✓	c		
98.0	0.030	RG	FRII	HERG		c-x	l	l
99.0	0.426	SEY	...	Sy2		c		
103.0	0.33	RG	FRII			c		
105.0	0.089	RG	FRII	HERG		c-x	k;h	
107.0	0.785	RG	FRII	HERG		c	e	
109.0	0.307	RG	FRII	HERG		c-x	h;l	
111.0	0.049	RG	FRII			c-x	k;h	
114.0	0.815	RG	FRII	LERG		c		
119.0	1.023	QSO	CSS			c		
123.0	0.218	RG	FRII	LERG	✓	c	h;igm	
124.0	1.083	RG	FRII	HERG		c	l	
125.0	?	UNID				
129.0	0.021	RG	FRI-NAT		✓	c-x	k;igm	igm
129.1	0.022	RG	FRI		✓	c-x	igm	igm
130.0	0.109	RG	FRI-WAT		✓	c	e	
131.0	?	UNID				
132.0	0.214	RG	FRII	LERG	✓	c-x		
133.0	0.278	RG	FRII	HERG		c		
134.0	?	UNID				
135.0	0.127	RG	FRII	HERG	✓	c		
136.1	0.064	RG	FRII-XS	HERG		c	e	
137.0	?	UNID				
138.0	0.759	QSO	CSS			c		
139.2	?	UNID				
141.0	?	UNID				
142.1	0.406	RG	FRII			c		
147.0	0.545	QSO	CSS			c		
152.0	?	UNID				
153.0	0.277	RG	FRII	LERG	✓	c-x		
154.0	0.58	QSO				c	e;k	
158.0	?	UNID				
165.0	0.296	RG	FRII	LERG		c	e	
166.0	0.245	RG	FRII	LERG		c		
169.1	0.633	RG	FRII	HERG		c		
171.0	0.238	RG	FRII	HERG		c-x	e	
172.0	0.519	RG	FRII	HERG		c		
173.0	1.035	QSO	CSS	HERG		c		
173.1	0.292	RG	FRII	LERG	✓	c	h;l	
175.0	0.77	QSO				c		
175.1	0.92	RG	FRII	HERG		c		
180.0	0.22	RG	FRII	HERG		c		
181.0	1.382	QSO				c	h	
184.0	0.994	RG	FRII	HERG	✓	c-x	l	igm
184.1	0.118	RG	FRII	HERG	✓	c		
186.0	1.066	QSO	CSS		✓	c	igm	
187.0	0.465	RG	FRII	LERG		c	e;l	
190.0	0.246	QSO	CSS			c		
191.0	1.968	QSO				c	k;l	
192.0	0.060	RG	FRII-XS	HERG	✓	c-x	l	igm
194.0	1.184	RG	FRII	HERG		c		

Table 5
(Continued)

3CR ^a name	z ^b	Class ^c	Radio ^d morph.	Optical ^e class	Cluster ^f flag	X-Ray ^g obs.	<i>Chandra</i> ^h detections	<i>XMM-Newton</i> ⁱ detections
196.0	0.871	QSO				c		
196.1	0.198	RG		LERG	✓	c	igm	
197.1	0.128	RG		HERG	✓	c		
198.0	0.081	RG		HERG	✓	c		
200.0	0.458	RG		LERG	✓	c	k;l	
204.0	1.112	QSO				c-x		
205.0	1.532	QSO				c-x		
207.0	0.680	QSO	LDQ		✓	c-x	k;l	igm
208.0	1.112	QSO				c		
208.1	1.02	QSO				c-x		
210.0	1.169	RG	FRII	HERG	✓	c-x	e;h	igm
212.0	1.049	QSO	LDQ			c	e;h	
213.1	0.194	RG	FRI-CSS	LERG	✓	c	e;h	
215.0	0.411	QSO			✓	c-x	k;l	
216.0	0.670	QSO				c		
217.0	0.898	RG	FRII	HERG		c		
219.0	0.175	RG	FRII	HERG	✓	c	k;l	
220.1	0.61	RG	FRII	HERG	✓	c	igm	
220.2	1.156	QSO				c	h	
220.3	0.68	RG	FRII	HERG		c		
222.0	1.339	RG	FRI			c		
223.0	0.137	RG	FRII	HERG	✓	c-x		igm
223.1	0.108	RG	FRII-XS	HERG		c		
225A	1.565	RG	FRII	HERG		c		
225B	0.58	RG	FRII	HERG		c	h	
226.0	0.818	RG	FRII	HERG		c		
227.0	0.086	RG	FRII	HERG		c	h	
228.0	0.552	RG	FRII	HERG		c	e;h	
230.0	1.487	RG	FRII	HERG		c		
231.0	0.001	RG	FRI	LERG		c-x		
234.0	0.185	RG	FRII	HERG		c-x	h	
236.0	0.101	RG	FRII	LERG		c		
237.0	0.877	RG	FRII-CSS			c		
238.0	1.405	RG	FRII	HERG		c	h	
239.0	1.781	RG	FRII	HERG		x		
241.0	1.617	RG	FRII			c-x		
244.1	0.428	RG	FRII	HERG	✓	c-x	e	
245.0	1.028	QSO				c	k	
247.0	0.749	RG	FRII	HERG	✓	c		
249.0	1.554	QSO				x		
249.1	0.312	QSO				c-x		
250.0	?	UNID				
252.0	1.1	RG	FRII	HERG		c		
254.0	0.737	QSO	LDQ			c	e;h	
255.0	1.355	RG	FRII(?)	HERG		c		
256.0	1.819	RG	FRII	HERG		c		
257.0	2.474	QSO				x		
258.0	0.165	RG	FRI-CSS	LERG	✓	c		
263.0	0.646	QSO	LDQ			c	h	
263.1	0.824	RG	FRII	HERG		c		
264.0	0.022	RG	FRI	LERG	✓	c-x	k	igm
265.0	0.811	RG	FRII	HERG		c	h;l	
266.0	1.275	RG	FRII	HERG		c-x		
267.0	1.14	RG	FRII	HERG		c		
268.1	0.97	RG	FRII	HERG		c	h	
268.2	0.362	RG	FRII	HERG	✓	c-x	e;h	
268.3	0.372	RG	FRII-CSS			c		
268.4	1.402	QSO				c-x		
270.0	0.007	RG	FRI	LERG	✓	c-x	k	igm
270.1	1.528	QSO				c		
272.0	0.944	RG	FRII	HERG		c		
272.1	0.003	RG	FRI	LERG	✓	c-x	k	

Table 5
(Continued)

3CR ^a name	z^b	Class ^c	Radio ^d morph.	Optical ^e class	Cluster ^f flag	X-Ray ^g obs.	<i>Chandra</i> ^h detections	<i>XMM-Newton</i> ⁱ detections
273.0	0.158	QSO	CDQ			c-x	k	
274.0	0.004	RG	FRI	LERG	✓	c-x	k;igm	igm
274.1	0.422	RG	FRII	HERG		c-x	e	l
275.0	0.48	RG	FRII	LERG	✓	c		
275.1	0.555	QSO	LDQ			c	k;h;l	
277.0	0.414	RG	FRII			c		
277.1	0.320	QSO	CSS			c		
277.2	0.766	RG	FRII	HERG		c-x		
277.3	0.085	RG	FRII	HERG		c		
280.0	0.996	RG	FRII	HERG	✓	c-x	k;h;l	
280.1	1.667	QSO						
284.0	0.240	RG	FRII	HERG	✓	c-x		igm
285.0	0.080	RG	FRII	HERG		c	l	
286.0	0.850	QSO	CSS			c		
287.0	1.055	QSO	CSS			c-x		
287.1	0.216	RG	FRII	HERG		c	h	
288.0	0.246	RG	FRI	LERG	✓	c	igm	
288.1	0.963	QSO				c		
289.0	0.967	RG	FRII	HERG		c		
292.0	0.71	RG	FRII	HERG	✓	c-x	e	igm
293.0	0.045	RG	FRI	LERG		c	e	
293.1	0.709	RG	FRII			c		
294.0	1.779	RG	FRII	HERG	✓	c	h;igm	
295.0	0.464	RG	FRII	LERG	✓	c	h;igm	
296.0	0.025	RG	FRI	LERG	✓	c-x	k;igm	igm
297.0	1.406	QSO				c	k;e	
298.0	1.438	QSO	CSS		✓	c-x		igm
299.0	0.367	RG	FRII		✓	c	h	
300.0	0.27	RG	FRII	HERG		c-x		
300.1	1.159	RG	FRII	HERG		c		
303.0	0.141	RG	FRII	HERG	✓	c	k;l	
303.1	0.270	RG	FRII-CSS	HERG		c-x	e	
305.0	0.042	RG	FRII	HERG		c-x	e	
305.1	1.132	RG	FRII-CSS	LERG		c		
306.1	0.441	RG	FRII	HERG	✓	c	e	
309.1	0.905	QSO	CSS			c	e	
310.0	0.054	RG	FRI	LERG	✓	c	igm	
313.0	0.461	RG	FRII	HERG	✓	c	h;igm	
314.1	0.120	RG	FRI	LERG	✓	c-x		
315.0	0.108	RG	FRI-XS	LERG	✓	c	e	
317.0	0.034	RG	FRI	LERG	✓	c-x	igm	igm
318.0	1.574	RG	FRII-CSS		✓	c-x		
318.1	0.045	RG	FRI	LERG	✓	c-x	igm	igm
319.0	0.192	RG	FRII	LERG	✓	c-x		
320.0	0.342	RG	FRII	LERG	✓	c	igm	
321.0	0.096	RG	FRII	HERG		c-x	h;l	
322.0	1.681	RG	FRII	HERG	✓	x		igm
323.0	0.679	RG	FRII	HERG		c	e	
323.1	0.264	RG	FRII	HERG	✓	c		
324.0	1.206	RG	FRII	HERG	✓	c-x	e;h	
325.0	1.135	RG	FRII			c	h	
326.0	0.090	RG	FRII	LERG		c	l	
326.1	1.825	RG	FRII	HERG				
327.0	0.105	RG	FRII	HERG	✓	c	h	
327.1	0.462	RG	FRI	HERG		c-x	k	
330.0	0.55	RG	FRII	HERG	✓	c	h;l	
332.0	0.151	RG	FRII	HERG	✓	c		
334.0	0.555	QSO	LDQ			c	k;l	
336.0	0.927	QSO				c		
337.0	0.635	RG	FRII	HERG	✓	c-x	e	
338.0	0.030	RG	FRI	LERG	✓	c-x	igm	igm
340.0	0.775	RG	FRII	HERG		c		







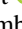
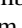
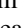
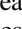

Table 5
(Continued)

3CR ^a name	z^b	Class ^c	Radio ^d morph.	Optical ^e class	Cluster ^f flag	X-Ray ^g obs.	<i>Chandra</i> ^h detections	<i>XMM-Newton</i> ⁱ detections
341.0	0.448	RG	FRII	HERG	✓	c-x	e;k	igm
343.0	0.988	QSO	CSS			c		
343.1	0.75	RG	FRII-CSS			c		
345.0	0.593	QSO	CDQ		✓	c-x	k	igm
346.0	0.162	RG	FRI	HERG	✓	c	k	
348.0	0.155	RG	FRI	LERG	✓	c-x	igm	igm
349.0	0.205	RG	FRII	HERG		c-x	h	
351.0	0.372	RG	FRII			c	h	
352.0	0.807	RG	FRII	HERG		c		
353.0	0.030	RG	FRII	LERG	✓	c-x	k;l:igm	igm
356.0	1.079	RG	FRII	HERG		c	e	
357.0	0.166	RG	FRII	LERG	✓	c		
368.0	1.131	RG	FRII	HERG		c		
371.0	0.051	BL		-		c	k	
379.1	0.256	RG	FRII-XS	HERG		c		
380.0	0.692	QSO	CDQ			c	k	
381.0	0.161	RG	FRII	HERG		c		
382.0	0.058	RG	FRII	HERG		c-x		
386.0	0.017	RG	FRI	LERG	✓	c-x		igm
388.0	0.092	RG	FRII	LERG	✓	c	e	
389.0	?	UNID		x		
390.0	?	UNID				
390.3	0.056	RG	FRII	HERG		c-x	k;h	
394.0	?	UNID				
399.1	?	UNID				
401.0	0.201	RG	FRII	LERG	✓	c	igm	
402.0	0.026	RG	FRI		✓	c-x	k	
403.0	0.059	RG	FRII-XS	HERG		c	k;h	
403.1	0.055	RG	FRII	LERG	✓	c		
405.0	0.056	RG	FRII		✓	c-x	h;igm	igm
409.0	?	UNID				
410.0	0.249	RG	FRII			c		
411.0	0.467	RG	FRII	HERG		c-x		
415.2	?	UNID				
418.0	1.686	QSO						
424.0	0.127	RG	FRI	LERG	✓	c	e	
427.1	0.572	RG	FRII	LERG	✓	c	l;igm	
428.0	?	UNID				
430.0	0.056	RG	FRII	LERG	✓	c	e	
431.0	?	UNID				
432.0	1.785	QSO				c-x		
433.0	0.102	RG	FRII-XS	HERG		c	l	
434.0	0.322	RG	FRII	LERG	✓	c		
435.0	0.471	RG	FRII	HERG		c		
436.0	0.215	RG	FRII	HERG		c-x	e;h	
437.0	1.48	RG	FRII	HERG		c	e;h	
438.0	0.29	RG	FRII	HERG	✓	c	igm	
441.0	0.708	RG	FRII	HERG		c		
442.0	0.026	RG	FRI	LERG	✓	c	igm	
445.0	0.056	RG	FRII		✓	c-x	h	
449.0	0.017	RG	FRI	LERG	✓	c-x	igm	igm
452.0	0.081	RG	FRII	HERG	✓	c-x	h;l	igm
454.0	1.757	QSO	CSS			x		
454.1	1.841	RG	FRII-CSS		✓			
454.2	?	UNID				
454.3	0.859	QSO	CDQ			c-x	k	
455.0	0.543	QSO	CSS			c		
456.0	0.233	RG	FRII	HERG		c		
458.0	0.289	RG	FRII	HERG	✓	c	h	
459.0	0.220	RG	FRII	HERG		c-x	l	
460.0	0.268	RG	FRII	LERG	✓	c-x		
465.0	0.030	RG	FRI-WAT	LERG	✓	c-x	k;igm	igm

Table 5
(Continued)

3CR ^a name	<i>z</i> ^b	Class ^c	Radio ^d morph.	Optical ^e class	Cluster ^f flag	X-Ray ^g obs.	<i>Chandra</i> ^h detections	<i>XMM-Newton</i> ⁱ detections
468.1	?	UNID				
469.1	1.336	RG	FR II	HERG		c-x		1
470.0	1.653	RG	FR II			c	h	

Notes.^a The 3CR name.^b Redshift *z*. We also verified in the literature (e.g., NED/IPAC or SIMBAD databases) if updated *z* values were reported after the release of the 3CR catalog.^c Source classification: RG stands for radio galaxies, QSO for quasars, Sy for Seyfert galaxies, and BL for BL Lac objects. We used the acronym UNID for sources that are still unidentified.^d Radio morphological classification: FR I and FR II refer to the Fanaroff and Riley classification criterion (Fanaroff & Riley 1974), while LDQ and CDQ are sometimes adopted for lobe-dominated and core-dominated quasars; we also indicated if in the literature the source is classified as CSS or if the radio structure is X-shaped (XS), or if it is a narrow or wide angle tailed radio galaxy (NAT and WAT, respectively).^e Optical spectroscopic designation: LERG for low-excitation radio galaxy and HERG for high-excitation radio galaxy.^f The “cluster flag” marks sources for which there is a known optical group/cluster reported in the literature or those for which there is an archival X-ray observation indicating the presence of hot gas.^g The “c” flag indicates that at least one *Chandra* observation is present in its archive, while the “x” flag refers to the *XMM-Newton* archive.^h In this column we report if the source has a radio component with an X-ray counterpart in a *Chandra* observation. We used the following labels: k = jet knot, h = hotspot, l = lobe, e = extended X-ray emission around the nucleus, and igm = emission associated with the presence of hot gas.ⁱ The same as the previous column but for the *XMM-Newton* observations; we used only l and igm.**ORCID iDs**

C. Stuardi  <https://orcid.org/0000-0003-1619-3479>
 F. Massaro  <https://orcid.org/0000-0002-1704-9850>
 F. Ricci  <https://orcid.org/0000-0001-5742-5980>
 E. Liuzzo  <https://orcid.org/0000-0003-0995-5201>
 A. Paggi  <https://orcid.org/0000-0002-5646-2410>
 R. P. Kraft  <https://orcid.org/0000-0002-0765-0511>
 G. R. Tremblay  <https://orcid.org/0000-0002-5445-5401>
 S. A. Baum  <https://orcid.org/0000-0002-4735-8224>
 C. P. O’Dea  <https://orcid.org/0000-0001-6421-054X>
 B. J. Wilkes  <https://orcid.org/0000-0003-1809-2364>
 W. R. Forman  <https://orcid.org/0000-0002-9478-1682>

References

- Albaret, F. D., Prieto, A., Almeida, A., et al. 2017, *ApJS*, **233**, 25
 Arnaud, K. A. 1996, in ASP Conf. Ser. 101, *Astronomical Data Analysis Software and Systems V*, ed. G. Jacoby & J. Barnes (San Francisco, CA: ASP), 17
 Balmaverde, B., Capetti, A., Grandi, P., et al. 2012, *A&A*, **545**, A143
 Belsole, E., Worrall, D. M., Hardcastle, M. J., & Croston, J. H. 2007, *MNRAS*, **381**, 1109
 Bennett, C. L., Larson, D., Weiland, J. L., & Hinshaw, G. 2014, *ApJ*, **794**, 135
 Buttiglione, S., Capetti, A., Celotti, A., et al. 2009, *A&A*, **495**, 1033
 Buttiglione, S., Capetti, A., Celotti, A., et al. 2011, *A&A*, **L525**, 28
 Croston, J. H., Hardcastle, M. J., Birkinshaw, M., Worrall, D. M., & Laing, R. A. 2008, *MNRAS*, **386**, 1709
 Croston, J. H., Hardcastle, M. J., Harris, D. E., et al. 2005, *ApJ*, **626**, 733
 Dasadia, S., Sun, M., Morandi, A., et al. 2016, *MNRAS*, **458**, 681
 Davis, J. E. 2001, *ApJ*, **562**, 575
 Dicken, D., Tadhunter, C., Morganti, R., et al. 2014, *ApJ*, **788**, 98
 Djorgovski, S., Spinrad, H., McCarthy, P., et al. 1988, *AJ*, **96**, 836
 Dunlop, J. S., & Peacock, J. A. 1993, *MNRAS*, **263**, 936
 Eracleous, M., & Halpern, J. P. 1994, *ApJS*, **90**, 1
 Evans, D. A., Worrall, D. M., Hardcastle, M. J., Kraft, R. P., & Birkinshaw, M. 2006, *ApJ*, **642**, 96
 Fabian, A. C. 2012, *ARAA*, **50**, 455
 Fanaroff, B. L., & Riley, J. M. 1974, *MNRAS*, **167**, P31
 Fanti, C., Fanti, R., Schilizzi, R. T., Spencer, R. E., & van Breugel, W. J. M. 1986, *A&A*, **170**, 10
 Fermi, I. 2014, *ApJS*, **212**, 19
 Freeman, P., Doe, S., & Siemiginowska, A. 2001, *Proc. SPIE*, **4477**, 76
 Ghaffari, Z., Westhues, C., Haas, M., et al. 2017, *AN*, **338**, 823
 Giraud, E. 1990, *A&A*, **234**, 20
 Giraud, E. 1991, *A&A*, **253**, L5
 Hardcastle, M. J., Massaro, F., & Harris, D. E. 2010, *MNRAS*, **401**, 2697
 Hardcastle, M. J., Massaro, F., Harris, D. E., et al. 2012, *MNRAS*, **424**, 1774
 Heckman, T. M., O’Dea, C. P., Baum, S. A., & Laurikainen, E. 1994, *ApJ*, **428**, 65
 Hewitt, A., & Burbidge, G. 1991, *ApJS*, **75**, 297
 Hilbert, B., Chiaberge, M., Kotyla, J. P., et al. 2016, *ApJS*, **225**, 12
 Hiltner, P. R., & Röser, H. J. 1991, *A&A*, **244**, 37
 Ineson, J., Croston, J. H., Hardcastle, M. J., et al. 2013, *ApJ*, **770**, 136
 Ineson, J., Croston, J. H., Hardcastle, M. J., & Mingo, B. 2017, *MNRAS*, **467**, 1586
 Jackson, N., & Rawlings, S. 1997, *MNRAS*, **286**, 241
 Kalberla, P. M. W., Burton, W. B., Hartmann, D., et al. 2005, *A&A*, **440**, 775
 Kotyla, J. P., Chiaberge, M., Baum, S., et al. 2016, *ApJ*, **826**, 46
 Kraft, R. P., Birkinshaw, M., Nulsen, P. E. J., et al. 2012, *ApJ*, **749**, 19
 Laskar, T., Fabian, A. C., Blundell, K. M., & Erlund, M. C. 2010, *MNRAS*, **401**, 1500
 Law-Green, J. D. B., Leahy, J. P., Alexander, P., et al. 1995, *MNRAS*, **274**, 939
 Le Fèvre, O., & Hammer, F. 1990, *ApJ*, **350**, 1
 Le Fèvre, O., Hammer, F., & Jones, J. 1988, *ApJ*, **331**, 73
 Leipski, C., Haas, M., Willner, S. P., et al. 2010, *ApJ*, **717**, 766
 Mannering, E., Worrall, D. M., & Birkinshaw, M. 2013, *MNRAS*, **431**, 858
 Mantovani, F., Rossetti, A., Junor, W., Saikia, D. J., & Salter, C. J. 2010, *A&A*, **518**, 33
 Maselli, A., Massaro, F., Cusumano, G., et al. 2016, *MNRAS*, **460**, 3829
 Massaro, F., Chiaberge, M., Grandi, P., et al. 2009a, *ApJL*, **692**, L123
 Massaro, F., Harris, D. E., & Cheung, C. C. 2011, *ApJS*, **197**, 24
 Massaro, F., Harris, D. E., Chiaberge, M., et al. 2009b, *ApJ*, **696**, 980
 Massaro, F., Harris, D. E., Liuzzo, E., et al. 2015, *ApJS*, **220**, 5
 Massaro, F., Harris, D. E., Tremblay, G. R., et al. 2010, *ApJ*, **714**, 589
 Massaro, F., Harris, D. E., Tremblay, G. R., et al. 2013, *ApJS*, **206**, 7
 Massaro, F., Missaglia, V., Stuardi, C., et al. 2018, *ApJS*, **234**, 7
 Massaro, F., Tremblay, G. R., Harris, D. E., et al. 2012, *ApJS*, **203**, 31
 McCarthy, P. J. 1989, PhD thesis, Univ. California
 McCarthy, P. J., Miley, G. K., de Koff, S., et al. 1997, *ApJS*, **112**, 415
 Nan, R., Gabuzda, D. C., Kamenov, S., Schilizzi, R. T., & Inoue, M. 1999, *A&A*, **344**, 402
 O’Dea, C. P. 1998, *PASP*, **110**, 493
 O’Dea, C. P., Worrall, D. M., Tremblay, G. R., et al. 2017, *ApJ*, **851**, 87
 Park, T., Kashyap, V. L., Siemiginowska, A., et al. 2006, *ApJ*, **652**, 610
 Pauliny-Toth, I. I. K., & Kellermann, K. I. 1968, *AJ*, **73**, 953
 Podigachoski, P., Rocca-Volmerange, B., Barthel, P., Drouart, G., & Fioc, M. 2016, *MNRAS*, **462**, 4183
 Privon, G. C., O’Dea, C. P., & Baum, S. A. 2008, *ApJS*, **175**, 423

- Ramírez, E. A., Tadhunter, C. N., Dicken, D., et al. 2014, *MNRAS*, **439**, 1270
- Roland, J., Véron, P., Stannard, D., & Muxlow, T. 1982, *A&A*, **116**, 60
- Salter, C. J., & Haslam, C. G. T. 1980, *A&A*, **81**, 240
- Shelton, D. L., Hardcastle, M. J., & Croston, J. H. 2011, *MNRAS*, **418**, 811
- Shields, G. A. 1999, *PASP*, **111**, 661
- Shih, H., Stockton, A., & Kewley, L. 2013, *ApJ*, **772**, 138
- Spinrad, H., Marr, J., Aguilar, L., & Djorgovski, S. 1985, *PASP*, **97**, 932
- Steinbring, E. 2011, *AJ*, **142**, 172
- Strom, R. G., Riley, J. M., Spinrad, H., et al. 1990, *A&A*, **227**, 19
- Tadhunter, C. 2016, *A&ARv*, **24**, 10
- Taylor, G. B., Inoue, M., & Tabara, H. 1992, *A&A*, **264**, 415
- Taylor, M. B. 2005, in ASP Conf. Ser. 347, *Astronomical Data Analysis Software and Systems XIV*, ed. P. Shopbell, M. Britton, & R. Ebert (San Francisco, CA: ASP), 29
- Tremblay, G. R., Chiaberge, M., Sparks, W. B., et al. 2009, *ApJS*, **183**, 278
- Tyul'bashev, S. A., & Chernikov, P. A. 2000, *ARep*, **44**, 286
- van Breugel, W. J. M., Fanti, C., Fanti, R., et al. 1992, *A&A*, **256**, 56
- Wilkes, B. J., Kuraszkiewicz, J., Haas, M., et al. 2013, *ApJ*, **773**, 15
- Wright, E. L., Eisenhardt, P. R. M., Mainzer, A. K., et al. 2010, *AJ*, **140**, 1868